



室蘭工業大学

学術資源アーカイブ

Muroran Institute of Technology Academic Resources Archive



曇り度の自己調整によるヘイズ除去に関する研究

メタデータ	言語: eng 出版者: 公開日: 2015-06-11 キーワード (Ja): キーワード (En): 作成者: 毛, 鈞 メールアドレス: 所属:
URL	https://doi.org/10.15118/00005126

MURORAN INSTITUTE OF TECHNOLOGY

DOCTORAL THESIS

**Study on Image Dehazing with the
Self-Adjustment of the Haze Degree**

Author:

Jun MAO

Student ID:12092002

Supervisor:

Prof. Hiroyuki SHIOYA

*A thesis submitted in fulfilment of the requirements
for the degree of Doctor of Engineering*

in the

Division of Production and Information Systems Engineering

February 2015

Declaration of Authorship

I, Jun MAO

Student ID:12092002, declare that this thesis titled, 'Study on Image Dehazing with the Self-Adjustment of the Haze Degree ' and the work presented in it are my own. I confirm that:

- This work was done wholly or mainly while in candidature for a research degree at this University.
- Where any part of this thesis has previously been submitted for a degree or any other qualification at this University or any other institution, this has been clearly stated.
- Where I have consulted the published work of others, this is always clearly attributed.
- Where I have quoted from the work of others, the source is always given. With the exception of such quotations, this thesis is entirely my own work.
- I have acknowledged all main sources of help.
- Where the thesis is based on work done by myself jointly with others, I have made clear exactly what was done by others and what I have contributed myself.

Signed:

Date:

MURORAN INSTITUTE OF TECHNOLOGY

Abstract

Doctor of Engineering

Study on Image Dehazing with the Self-Adjustment of the Haze Degree

by Jun MAO

Student ID:12092002

With the increase in industrial production and human activities, the concentration of atmospheric particulate matter (PM) is substantially increased, leading to fog and haze occurs more frequently. Limited visibility caused by suspended particles in the air, such as fog and haze, is a major problem for many applications of computer vision. The captured scenes by such computer vision systems suffer from poor visibility, low contrast, dimmed brightness, low luminance and distorted color, which makes detection of objects within the scene more difficult. Therefore visibility improvement, contrast and features enhancement of images and videos captured in bad weather, also called as dehazing, is an inevitable task. Furthermore, estimated actual weather condition is a valuable information to invoke corresponding approaches.

Haze removal is a difficult problem due to the inherent ambiguity between the haze and the underlying scene. Model-based single image dehazing methods are physically sound and produce qualitatively good results, however, more attentions to dehazing quality rather than the applicability leads to for real-time applications they may not always be fast enough, besides, there exist limitations such as color-bias and unable to deal with the sky area , etc.

The objectives of this study are to automatically estimate the haze degree from single image and label the image a haze factor, to propose a self-adjustment dehazing method due to the haze degree and to evaluate the performance of the dehazing method.

In this research, based on the atmospheric scattering model analysis and the statistics of various outdoor images, the following conclusions can be drawn: clear-day images have higher contrast than images plagued by bad weather; in most of the local regions even the sky, hazed images have larger minimum values of most color channel (RGB) pixels closing to airlight value. Relying on these two observations, an estimate function to label the foggy image with different haze degrees is developed which is related to haze removal constant parameter. In order to reduce the computational cost while providing the promising dehazed results also for real-time applications, by modifying the dark channel prior, the transmission estimation is carried out by obtaining the minimum value from only the relevant pixel itself or the mean filter of minimum values of its neighboring pixels.

The main advantage of the proposed algorithm compared with others is its processing speed: its complexity is a linear function of the number of image pixels, because of only performing mean filter once to estimate the final transmission map. Another advantage is similar image processing quality with Dark Channel Prior method. Further, labeling images different haze-degree can makes images-set mixed with haze and haze-free images batch processing possible. At last, the haze removal degree can be adaptive adjusted by a built-in function which makes the dehazed images look more natural.

Experiments are designed to test the haze degree estimate function using simulated images and real photographs. The proposed algorithm was also compared to other known haze removal methods, the experimental results clearly indicate that our approach achieves good performance on enhanced visibility, processing speed and stability, which makes our method applicable for real-time requirement.

Contents

Declaration of Authorship	i
Abstract	ii
Contents	iv
List of Figures	vi
List of Tables	viii
1 Introduction	1
1.1 Problem Statement	1
1.2 Motivation	4
1.3 Thesis goal	6
2 Background	7
2.1 Digital image basics	7
2.1.1 pixel	7
2.1.2 RGB color model	8
2.1.3 Channels of digital image	8
2.2 Edge detection	9
2.2.1 A simple edge model	11
2.2.2 Approaches of edge detection	12
2.2.3 Canny edge detection	12
2.2.4 Process of Canny edge detection algorithm	13
2.3 Basics of the Atmosphere	14
2.3.1 composition of air	16
2.3.2 Rayleigh scattering	18
2.3.3 Mie Scattering	20
2.4 Degradation Model	20
2.4.1 Attenuation of power	21
2.4.2 Sky intensity	22
2.4.3 Combining scattering effects	23
3 Previous Work of Dehazing	25

3.1	Overview of dehazing method	25
3.2	Non-Model-Based dehazing method	27
3.2.1	Gamma Correction	28
3.2.2	Histogram Equalisation	29
3.2.3	Unsharp Masking	31
3.3	model-based multi-image or intervention-required dehazing methods	32
3.3.1	Visibility Improvement Based on Polarization Filtered Images	32
3.3.2	The Deep Photo System	36
3.4	model-based single image dehazing methods	37
3.4.1	Fattals Method	37
3.4.2	Tan's Method	38
3.4.3	Dark Channel Prior	39
4	Detecting Foggy Images and Estimating the Haze Degree Factor	42
4.1	Atmospheric Scattering Model Analysis	43
4.2	Haze Degree Estimation Function	45
4.3	Experimental Results	47
4.4	Conclusions	49
5	Self-adjusting and Real-time Dehazing	51
5.1	Estimating the Transmission and Recovering the Scene Radiance	52
5.2	Algorithms and Complexity	53
5.3	Experimental Results and Analysis	53
5.3.1	Image restoration quality	54
5.3.2	Enhanced edge detection	59
5.3.3	Processing time cost	59
5.3.4	Effects of Different scenarios	59
5.4	Application of dehazing and symmetry detection	61
5.4.1	Definition of $D(AA')$	62
5.4.2	Details of A and A'	63
5.5	Conclusion	64
6	Conclusions and future work	67
6.1	conclusions	67
6.2	future work	68
	Acknowledgements	75

List of Figures

1.1	Global satellite-derived map of PM2.5 averaged over 2001-2006.	2
1.2	High PM2.5 concentration in Beijing and poor visibility caused by haze .	3
1.3	Images shows the hazy input image and the dehazed result	4
2.1	The range of intensity values from 0 (black) to 255 (white).	8
2.2	A digital grayscale image. The dimensions of this image is 512 rows by 768 columns and pixel intensity values of the 15×15 pixel portion of the image	9
2.3	Composition of RGB from 3 Grayscale images.	10
2.4	Dehazed output of Fig.1.2(b) by our dehazing method	15
2.5	Canny edge detection of Fig.1.2(b)	15
2.6	Canny edge detection of Fig.1.2(b) dehazed output	16
2.7	Major constituents of dry air, by volume	17
2.8	Airborne particulate size and wavelength of visible spectrum	18
2.9	Scattering of Light by small particles and molecules in the atmosphere .	19
2.10	Mie scattering Compare with Rayleigh scattering	19
2.11	Rayleigh and Mie Scattering	21
2.12	Light travels from an object to a observer through the air and sky intensity under uniform illumination(sunlight)	22
3.1	Comparison of computed images from the same input image created with different dehazing techniques.	27
3.2	Comparison of five Dehazing algorithm	28
3.3	Plot shows the principle of gamma correction and sample images	29
3.4	Comparison of both the histograms and images before histogram equal- ization and after	30
3.5	Simplified principle of unsharp masking	31
3.6	Model for polarisation-based dehazing.	32
3.7	Example for polarisation-based dehazing.	35
4.1	Sample dehazing flows by using haze degree estimation, where ω is a haze factor we defined	43
4.2	Atmospheric Scattering model used	44
4.3	Sample images from our database	46
4.4	$A_0 - d$ (horizontal axis) and c (vertical axis) of images from six groups. Larger points correspond to higher haze grades.	48
4.5	Sample images from FRIDA Database	48
4.6	Estimated haze factor ω of the five sets of FRIDA, the horizontal axis is Image No. (1 - 18) and the vertical axis is the haze-factor ω	49

4.7	Estimated haze factor ω of real images divided in three groups and their sample images with the haze factor on the right.	49
5.1	Algorithm flow of our dehazing method	54
5.2	Sample images from the FRIDA Database	59
5.3	Sample application of Dehazing and Symmetry detection	65

List of Tables

1.1	International Visibility Code with Meteorological Range	5
2.1	Particles Responsible for Atmospheric Scattering	17
4.1	Standards dividing images into six groups	45
4.2	Haze-free sample images which have larger $A_0 - d$ and c and haze samples have smaller ones.	47
5.1	Our method's image restoration quality compare to others'	55
5.2	Our method's image restoration quality compare to others'	56
5.3	Our method's image restoration quality compare to others'	57
5.4	Our method's image restoration quality compare to He's	58
5.5	Our method's image enhanced edge detection affection compare to others'	60
5.6	Our method's image enhanced edge detection affection compare to others'	61
5.7	Our method's image enhanced edge detection affection compare to others'	62
5.8	Processing time cost compare to He's	65
5.9	Effects of Different scenarios	66

Dedicated to my grandfather in heaven, who was forcibly conscripted by government of the Republic of China during the Second World War. His combat experience included battle of Guangzhou during War of Resistance, Liaoshen campaign in the war of liberation and then joined the people's Liberation Army, all the way from the northeast of China until the liberation of Hainan Island, the almost southeast of China. After the war , he gave up the sword for the plough. My total childhood accompanied by his breathtaking war stories and I always remember his words " If I can survive from my adventure is a miracle, I hope your future adventure will have more joy and fun." Thanks to this time of peace, I really did.

Chapter 1

Introduction

1.1 Problem Statement

One of the most serious environmental problems in the world is air pollution. Air pollution can be defined broadly as the introduction of chemicals, particulate matter, or biological materials into the atmosphere that cause harm or discomfort to humans or other living organisms, or cause damage to the natural environment or built environment. Air pollutants come from a variety of natural and manmade sources. Natural sources can include windblown dust, and soot from wildfires. Manmade sources can include motor vehicles, electric utility or industrial fuel burning, cooking, and manufacturing operations. The industrial revolution — which began in Great Britain and spread to the rest of Europe, the USA and Japan in the 18th century, is still ongoing in developing country such as China and India — increased significantly the combustion of biomass and fossil fuels in urban centers, leading to substantial increase in the concentration of atmospheric particulate matter (PM) and global warming, see Fig.1.1 and Fig.1.2(a).

Particle pollution (also known as "particulate matter") in the air includes a mixture of solids and liquid droplets. Some particles are emitted directly; others are formed in the atmosphere when other pollutants react. Particles come in a wide range of sizes. Those less than 10 micrometers in diameter (PM₁₀) are so small that they can get into the lungs, potentially causing serious health problems. Ten micrometers is smaller than the width of a single human hair. Particles less than 2.5 micrometers in diameter (PM_{2.5}) are called "fine" particles. These particles are so small that they can be detected only with an electron microscope. Sources of fine particles include all types of combustion, including motor vehicles, power plants, residential wood burning, forest fires, agricultural burning, and some industrial processes. Particles between 2.5 and 10 micrometers in

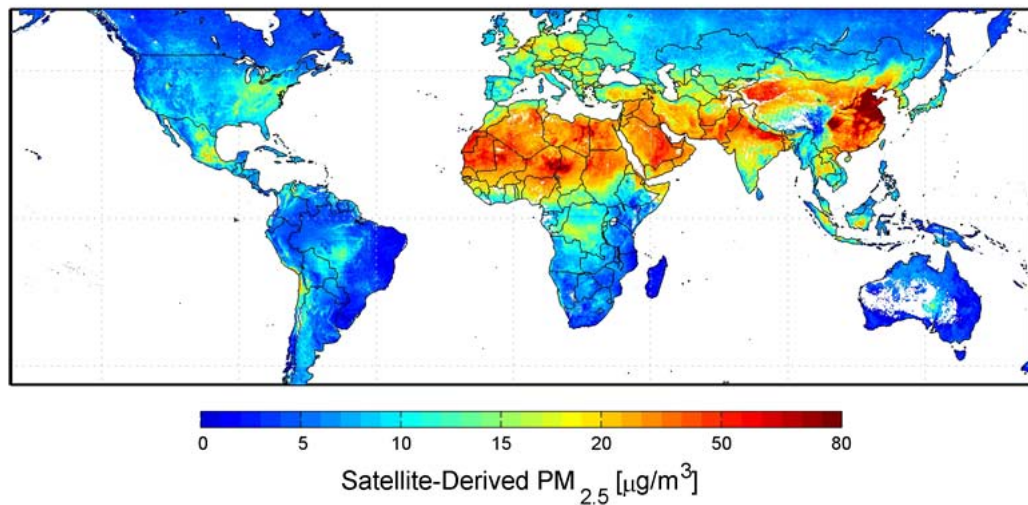
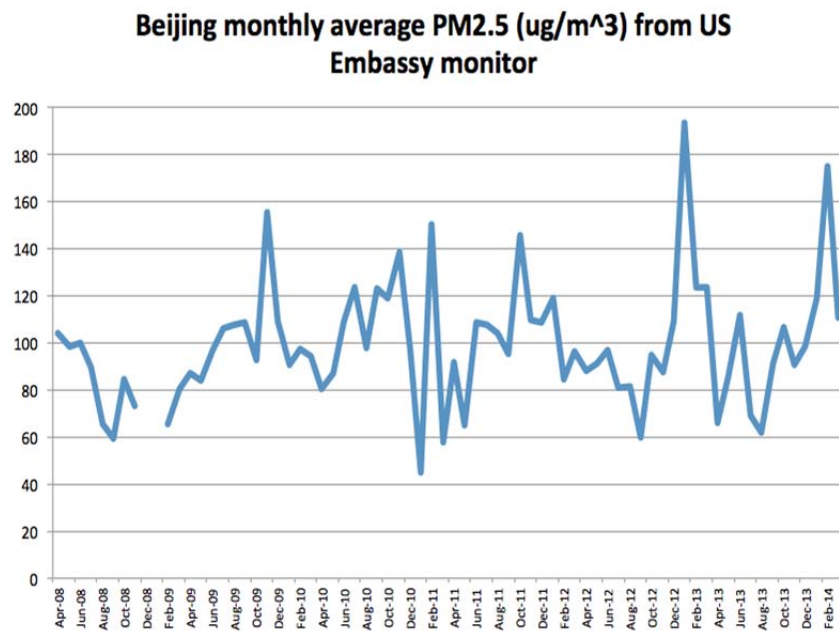


FIGURE 1.1: Global satellite-derived map of PM_{2.5} averaged over 2001-2006. Credit: Dalhousie University, Aaron van Donkelaar).

diameter are referred to as "coarse". Sources of coarse particles include crushing or grinding operations, and dust stirred up by vehicles traveling on roads.

One of the most basic forms of air pollution - haze - is the major cause of reduced visibility in many global cities and scenic areas, for instance, Beijing, see Fig.1.2(b), from Beijing environmental bureau's reports, Beijing only had 176 days with good air quality in 2013 . Haze is caused when sunlight encounters tiny particulate matter in the air, which reduce the clarity and color of what we see, and particularly during humid conditions.

Many outdoor computer vision applications like video surveillance, object detection, object recognition, tracking, intelligent vehicles and remote sensing systems etc. , assume that the input images have clear visibility. Unfortunately, this is not always true in many situations, in particular, haze and fog weather occurring more and more frequently. Outdoor images or videos are usually degraded by light scattering and absorbing from the aerosols, such as dust, mist, and fumes in the atmosphere, here regarded as haze. The captured scenes suffer from poor visibility, contrast, brightness, luminance and distorted color. With the help of Atmospheric optics theories, one can explain the effects that haze has on the visibility of a scene and eventually of an image taken of that scene. Moreover, with the development of computer graphics technology, it is possible to improve the visibility in terms of range, color verisimilitude and feature separation in digital images. Herein the term "dehazing" means to produce an image of a scene that does not contain haze effects although the source of that image originally comprised haze, for an example please refer to Fig.1.3.



(a) Beijing's month-average pm2.5 from 2008 to 2014



(b) Vehicles make their way along a road in poor visibility on a hazy day in Beijing

FIGURE 1.2: High PM2.5 concentration in Beijing and poor visibility caused by haze



FIGURE 1.3: Images show the hazy input image (parts of top left and bottom right) and the dehazed result (parts of top right and bottom left) using our dehazing Algorithm.

1.2 Motivation

A main objective in dehaze research is improvement of visibility and recovery of colors, as if imaging is done in clear conditions. Then Computer vision and human vision can process on such improved images for various applications, such as long range surveillance.

The need for image enhancement stems from the fact that the atmosphere is never free of particles. Even just pure air, the visual range has been found to be between 277km [1] to 348km [2], [3], not considering the curvature of the earth's surface. However, real visual ranges are much less than this theoretical value. The international visibility code for meteorological range rates visibilities between under 50m up to over 50km for

exceptionally clear air. These codes have been found to reflect a convenient scale for visual ranges in the daily work of meteorologists. For the exact codes please refer to Tab.1.1, the scattering coefficient

β_{sc} is an important parameter in visual range and will be dealt with in a separate section in this thesis(chapter 2).

TABLE 1.1: International Visibility Code with Meteorological Range

Code no.	Weather Condition	Meteorological Range, R_m	Scattering coefficient, $\beta_{sc}(km^{-1})$
0	Dense fog	50m	>78.2
1	Thick fog	50m - 200m	78.2 - 19.6
2	Moderate fog	200m - 500m	19.6 - 7.82
3	Light fog	500m - 1000m	7.82 - 3.91
4	Thin fog	1km - 2km	3.91 - 1.96
5	Haze	2km - 4km	1.96 - 0.954
6	Light haze	4km - 10km	0.954 - 0.391
7	Clear	10km - 20km	0.391 - 0.196
8	Very clear	20km - 50km	0.196 - 0.078
9	Exceptionally clear	>50km	0.078
-	Pure air	277km	0.0141

Source: [1]

In general, the haze-free image is more visually pleasing. Second, most computer vision algorithms, from low-level image analysis to high-level object recognition, usually assume that the input image (after radiometric calibration) is the scene radiance. The performance of computer vision algorithms(e.g., feature detection, filtering, and photometric analysis) will inevitably suffer from the biased, low-contrast scene radiance. Last, the haze removal can produce depth information and benefit many vision algorithms and advanced image editing. Haze or fog can be a useful depth clue for scene understanding. The bad haze image can be put to good use.

Significant progress in single image haze removal has been made in recent years. [4] made the observation that a haze-free image has higher contrast than a hazy image while assuming a smooth layer of airlight, and was able to obtain good results by maximizing contrast in local regions of the input image. However, the final results obtained by this method are not based on a physical model and yet may produce some halos near depth discontinuities in scene. [5] was able to obtain good results by assuming that transmission and surface shading are locally uncorrelated. With this assumption, he obtainsthe transmission map through independent component analysis. This approach is physically sound and can produce impressive results. However, it is deeply based on the color and thus cannot deal with a gray level image. The algorithm may fail in the cases when the locally uncorrelation of transmission and scene albedo is broken and is

computationally intensive. Lastly, a simple but powerful approach proposed by He et al.[3] who observed that the fact that objects in a clear image patch have at least one color channel with very low intensity, but in a hazy patch all color channels will have higher intensity due to airlight addition. Their method obtains results on a par with or exceeding other state-of-the-art algorithms, and is even successful with very hazy scenes. However, dark channel prior approach has two main drawbacks: (i) the soft matting in order to refine the transmission and remove halos near depth discontinuities in scene consumes a considerable amount of time and is hence not appropriate for real-time applications [6], it takes 10 to 20 seconds to restore a 600 x 400 image, (ii) due to the fixed haze removal constant parameter ω , the dehazed image may look over-dehazed, and transition between frames appears unnatural if using in video-dehazing.

Above all, we propose for a practical dehazing method, there are three problems to be solved: natural and consistent processed results between images, dehazing effect and processing speed.

1.3 Thesis goal

we aim to propose a simple and fast haze degree Estimate method which is based on two basic observations: haze-free images have more contrast than images plagued by bad weather; in most of the local regions even the sky, hazy images have larger minimum values of most color(RGB)channel pixels closing to airlight value. Relying on these two observations, we develop an estimate function related to haze removal constant parameter ω . In order to reduce the computational cost while providing the promising dehazed results also for real-time applications, by modifying the dark channel prior, the transmission estimation is carried out by obtaining the minimum value from only the relevant pixel itself or the median filter of minimum values of its neighboring pixels.

The first chapter after the introduction concerns with the basic of digital image and atmospheric Atmospheric Optics, followed by a chapter, which gives an overview of the dehazing methods that have been developed in recent years. In the fourth chapter detecting foggy images and estimating the haze degree method is described. Next, the author further describes the self-just dehazing algorithm using haze degree. The thesis finishes with a discussion and conclusion chapter.

Chapter 2

Background

2.1 Digital image basics

We have multiple ways to acquire digital images from the real world: digital cameras, scanners, computed tomography, and magnetic resonance imaging to name a few. In every case what humans see are images. However, when transforming this to our digital devices what we record are numerical values for each of the points of the image. The widespread availability of relatively low-cost personal computers has heralded a revolution in digital image processing activities among scientists and the consumer population in general.

2.1.1 pixel

In digital image, a pixel is a physical point in a raster image, or the smallest addressable element in an all points addressable display device; so it is the smallest controllable element of a picture represented on the screen. The address of a pixel corresponds to its physical coordinates. LCD pixels are manufactured in a two-dimensional grid, and are often represented using dots or squares, but CRT pixels correspond to their timing mechanisms and sweep rates. Each pixel is a sample of an original image; more samples typically provide more accurate representations of the original. A grayscale or greyscale digital image is an image in which the value of each pixel is a single sample, that is, it carries only intensity information. Images of this sort, also known as black-and-white, are composed exclusively of shades of gray, varying from black at the weakest intensity to white at the strongest. For most images, pixel values are integers that range from 0 (black) to 255 (white). The 256 possible gray intensity values are shown in Fig.2.1.

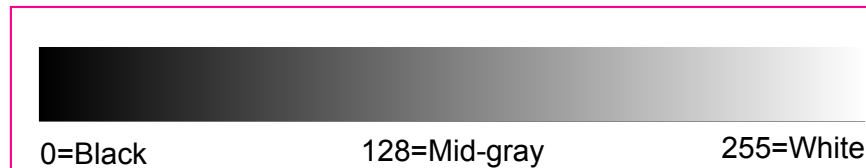


FIGURE 2.1: The range of intensity values from 0 (black) to 255 (white).

The intensity of each pixel is variable. In color image systems, a color is typically represented by three or four component intensities such as red, green, and blue (RGB color model), or cyan, magenta, yellow, and black (CMYK color model). For example in the Fig.2.2 you can see the 15×15 pixel block that represents the bottom left-hand corner of the image is nothing more than a matrix containing all the intensity values of the pixel points. How we get and store the pixels values may vary according to our needs, but in the end all images inside a computer world may be reduced to numerical matrices and other information describing the matrix itself.

2.1.2 RGB color model

The RGB color model is an additive color model in which red, green, and blue light are added together in various ways to reproduce a broad array of colors. The name of the model comes from the initials of the three additive primary colors, red, green, and blue.

The main purpose of the RGB color model is for the sensing, representation, and display of images in electronic systems, such as televisions and computers, though it has also been used in conventional photography. Before the electronic age, the RGB color model already had a solid theory behind it, based in human perception of colors.

2.1.3 Channels of digital image

Color digital images are made of pixels, and pixels are made of combinations of primary colors. A channel in this context is the grayscale image of the same size as a color image, made of just one of these primary colors. For instance, an image in RGB color model will have a red, green and blue channel. A grayscale image has just one channel.

Fig.2.3 is an example of color channel splitting of a full RGB color image. The column at left shows the isolated color channels in natural colors, while at right there are their grayscale equivalences:

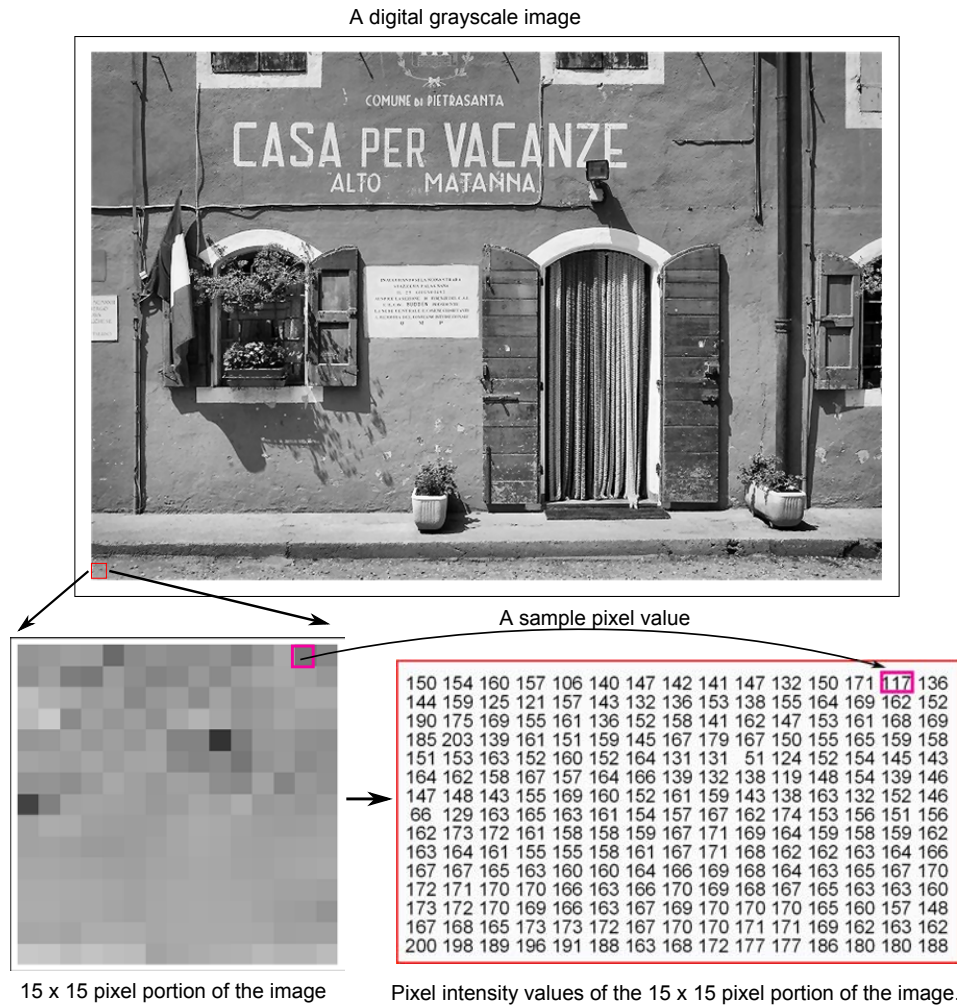


FIGURE 2.2: A digital grayscale image. The dimensions of this image is 512 rows by 768 columns. Thus the image is comprised of $512 \times 768 = 393,216$ pixels. Photo by Radka Tezaur. Bottom of the left hand is a 15×15 pixel portion of the image, right hand is the pixel intensity value matrix of the portion.

Source: <http://www.whymath.org/node/wavlets/imagebasics.html>

2.2 Edge detection

Edge detection is the name for a set of mathematical methods which aim at identifying points in a digital image at which the image brightness changes sharply or, more formally, has discontinuities. The points at which image brightness changes sharply are typically organized into a set of curved line segments termed edges. The same problem of finding discontinuities in 1D signals is known as step detection and the problem of finding signal discontinuities over time is known as change detection. Edge detection is a fundamental tool in image processing, machine vision and computer vision, particularly in the areas of feature detection and feature extraction.[7]

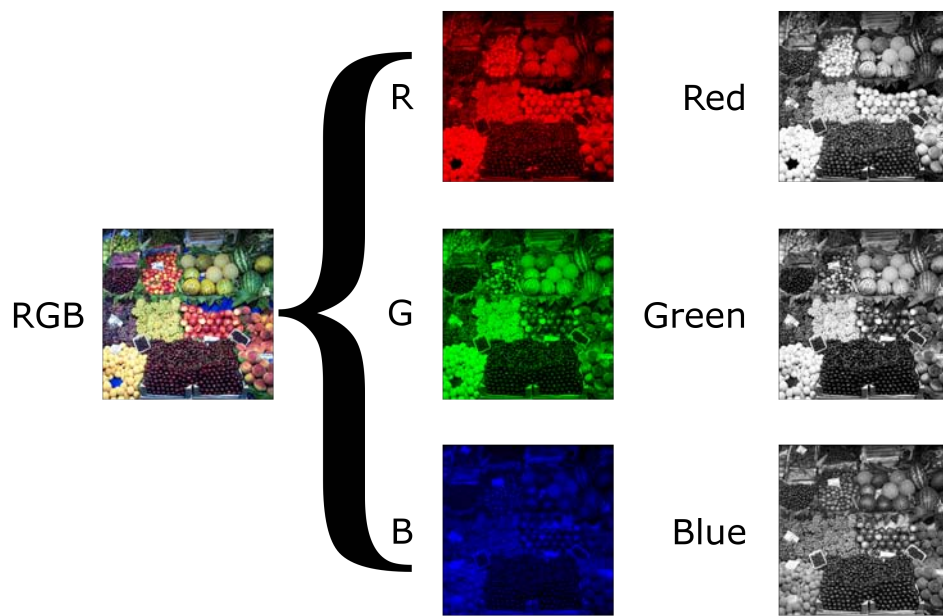


FIGURE 2.3: Composition of RGB from 3 Grayscale images.
Source: <http://en.wikipedia.org/wiki/Grayscalemediaviewer>

The purpose of detecting sharp changes in image brightness is to capture important events and changes in properties of the world. It can be shown that under rather general assumptions for an image formation model, discontinuities in image brightness are likely to correspond to:[8, 9]

- discontinuities in depth,
- discontinuities in surface orientation,
- changes in material properties and
- variations in scene illumination.

In the ideal case, the result of applying an edge detector to an image may lead to a set of connected curves that indicate the boundaries of objects, the boundaries of surface markings as well as curves that correspond to discontinuities in surface orientation. Thus, applying an edge detection algorithm to an image may significantly reduce the amount of data to be processed and may therefore filter out information that may be regarded as less relevant, while preserving the important structural properties of an image. If the edge detection step is successful, the subsequent task of interpreting the information contents in the original image may therefore be substantially simplified. However, it is not always possible to obtain such ideal edges from real life images of

moderate complexity. Edges extracted from non-trivial images are often hampered by fragmentation, meaning that the edge curves are not connected, missing edge segments as well as false edges not corresponding to interesting phenomena in the image thus complicating the subsequent task of interpreting the image data. Edge detection is one of the fundamental steps in image processing, image analysis, image pattern recognition, and computer vision techniques.

The edges extracted from a two-dimensional image of a three-dimensional scene can be classified as either viewpoint dependent or viewpoint independent. A viewpoint independent edge typically reflects inherent properties of the three-dimensional objects, such as surface markings and surface shape. A viewpoint dependent edge may change as the viewpoint changes, and typically reflects the geometry of the scene, such as objects occluding one another.

A typical edge might for instance be the border between a block of red color and a block of yellow. In contrast a line (as can be extracted by a ridge detector) can be a small number of pixels of a different color on an otherwise unchanging background. For a line, there may therefore usually be one edge on each side of the line.

2.2.1 A simple edge model

Although certain literature has considered the detection of ideal step edges, the edges obtained from natural images are usually not at all ideal step edges. Instead they are normally affected by one or several of the following effects:

- focal blur caused by a finite depth-of-field and finite point spread function.
- penumbral blur caused by shadows created by light sources of non-zero radius.
- shading at a smooth object.

A number of researchers have used a Gaussian smoothed step edge (an error function) as the simplest extension of the ideal step edge model for modeling the effects of edge blur in practical applications.[9, 10]

$$f(x) = \frac{\mathbf{I}_r - \mathbf{I}_l}{2} \left(\operatorname{erf}\left(\frac{x}{\sqrt{2}\sigma}\right) + 1 \right) + \mathbf{I}_l \quad (2.1)$$

At the left side of the edge, the intensity is $\mathbf{I}_l = \lim_{x \rightarrow -\infty} f(x)$, and right of the edge it is $\mathbf{I}_r = \lim_{x \rightarrow \infty} f(x)$. The scale parameter σ is called the blur scale of the edge.

2.2.2 Approaches of edge detection

There are many methods for edge detection, but most of them can be grouped into two categories, search-based and zero-crossing based. The search-based methods detect edges by first computing a measure of edge strength, usually a first-order derivative expression such as the gradient magnitude, and then searching for local directional maxima of the gradient magnitude using a computed estimate of the local orientation of the edge, usually the gradient direction. The zero-crossing based methods search for zero crossings in a second-order derivative expression computed from the image in order to find edges, usually the zero-crossings of the Laplacian or the zero-crossings of a non-linear differential expression. As a pre-processing step to edge detection, a smoothing stage, typically Gaussian smoothing, is almost always applied (see also noise reduction). The edge detection methods that have been published mainly differ in the types of smoothing filters that are applied and the way the measures of edge strength are computed. As many edge detection methods rely on the computation of image gradients, they also differ in the types of filters used for computing gradient estimates in the x - and y -directions.

2.2.3 Canny edge detection

John Canny considered the mathematical problem of deriving an optimal smoothing filter given the criteria of detection, localization and minimizing multiple responses to a single edge.[11] He showed that the optimal filter given these assumptions is a sum of four exponential terms. He also showed that this filter can be well approximated by first-order derivatives of Gaussians. Canny also introduced the notion of non-maximum suppression, which means that given the presmoothing filters, edge points are defined as points where the gradient magnitude assumes a local maximum in the gradient direction. Looking for the zero crossing of the 2nd derivative along the gradient direction was first proposed by Haralick.[12] It took less than two decades to find a modern geometric variational meaning for that operator that links it to the MarrHildreth (zero crossing of the Laplacian) edge detector. That observation was presented by Ron Kimmel and Alfred Bruckstein.[13] Although his work was done in the early days of computer vision, the Canny edge detector (including its variations) is still a state-of-the-art edge detector. Unless the preconditions are particularly suitable, it is hard to find an edge detector that performs significantly better than the Canny edge detector. The Canny-Deriche detector was derived from similar mathematical criteria as the Canny edge detector, although starting from a discrete viewpoint and then leading to a set of recursive filters for image smoothing instead of exponential filters or Gaussian filters.[14] The differential edge detector described below can be seen as a reformulation of Canny's method

from the viewpoint of differential invariants computed from a scale space representation leading to a number of advantages in terms of both theoretical analysis and sub-pixel implementation.

2.2.4 Process of Canny edge detection algorithm

The introduction of procedure below is developed based on OpenCV function Canny.

1. Convert color images to gray images if necessary.
2. Since edge detection is susceptible to noise in the image, first step is to remove the noise in the image with a Gaussian filter. For instance, a 5×5 Gaussian filter used to create the image to the right with $\sigma = 1.4$ is shown below. (The asterisk denotes a convolution operation.)

$$\mathbf{F}_\sigma = \frac{1}{159} \begin{pmatrix} 2 & 4 & 5 & 4 & 2 \\ 4 & 9 & 12 & 9 & 4 \\ 5 & 12 & 15 & 12 & 5 \\ 4 & 9 & 12 & 9 & 4 \\ 2 & 4 & 5 & 4 & 2 \end{pmatrix}$$

$$\mathbf{B} = \mathbf{F}_\sigma * \mathbf{A}$$

3. Computing derivatives of the image using vertical and horizontal Sobel Operator, so we get the derivatives along both x and y directions, based on which we can get the final gradient magnitude and the norm direction of the edge. We therefore have 2 images in this step, one derivative magnitude image and one image recording the gradient directions of corresponding pixels.

- Apply a pair of convolution masks (in x and y directions):

$$\mathbf{G}_x = \begin{pmatrix} -1 & 0 & 1 \\ -2 & 0 & 2 \\ -1 & 0 & 1 \end{pmatrix}$$

$$\mathbf{G}_y = \begin{pmatrix} -1 & -2 & -1 \\ 0 & 0 & 0 \\ 1 & 2 & 1 \end{pmatrix}$$

- Find the gradient strength and direction with:

$$\mathbf{G} = \sqrt{\mathbf{G}_x^2 + \mathbf{G}_y^2}$$

$$\theta = \arctan\left(\frac{\mathbf{G}_y}{\mathbf{G}_x}\right)$$

The direction is rounded to one of four possible angles (namely 0, 45, 90 or 135)

4. Non-maximum suppression is applied. For this, at every pixel, pixel is checked if it is a local maximum in its neighborhood in the direction of gradient. If so, it is considered for next stage, otherwise, it is suppressed (put to zero). This removes pixels that are not considered to be part of an edge. Hence, only thin lines (candidate edges) will remain.
5. Hysteresis: This stage decides which are all edges are really edges and which are not. For this, we need two threshold values, *minVal* (lower threshold) and *maxVal* (upper threshold).
 - If a pixel gradient is higher than the upper threshold, the pixel is accepted as an edge.
 - If a pixel gradient value is below the lower threshold, then it is rejected.
 - If the pixel gradient is between the two thresholds, then it will be accepted only if it is connected to a pixel that is above the upper threshold.

Canny recommended a upper:lower ratio between 2:1 and 3:1. So what we finally get is strong edges in the image.

More edges could be found in dehazed images is believed and illustrated by results of Canny edge detector of Fig.1.2(b) and dehazed output.

2.3 Basics of the Atmosphere

As light travels through a medium, it will most likely get altered due to interactions with the particles of that medium if the travel distance through that medium is sufficiently long. Reflections, scattering or absorption may happen depending on various factors of the medium. Due to these effects, it is plausible to conclude that light can't travel endlessly through a medium and especially not undistorted. To understand how exactly the atmosphere alters incident light, one must have a closer look at the composition of air and the atmosphere. This section will give a broad overview of the composition of the atmosphere and the origination of particles. The author will conclude the section with an observation of special atmospheric conditions such as fog and clouds.



FIGURE 2.4: Dehazed output of Fig.1.2(b) by our dehazing method



FIGURE 2.5: Canny edge detection of Fig.1.2(b), $minVal = 50, maxVal = 120, kernelSize = 3$

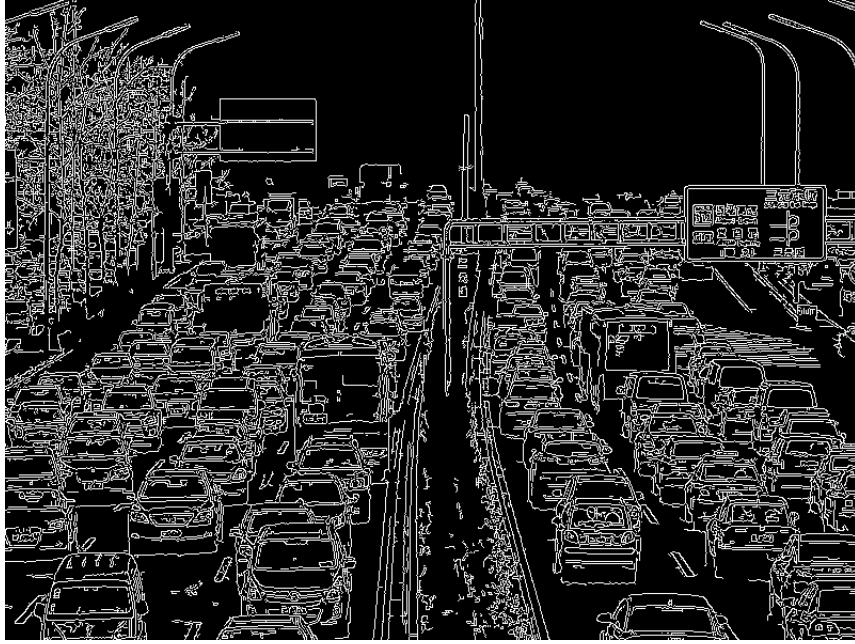


FIGURE 2.6: Canny edge detection of Fig.1.2(b) dehazed output, $minVal = 50, maxVal = 120, kernelSize = 3$

2.3.1 composition of air

Visibility is among other things dependent on the type of atoms, molecules and particles, in the field of view as well as their number and size distribution. In the simplest of cases, only pure air is present in the observed atmosphere. Although it is convenient for some research issues to introduce the concept of pure air, this is only a theoretical construct that marks the upper boundary of visibility in the atmosphere. Pure air only contains molecules with molecule sizes of $10^{-4}\mu m$ in radius and a concentration of about 10^{19} per cm^3 . The common name given to the atmospheric gases used in breathing and photosynthesis is air. By volume shown in Fig.2.7, dry air contains 78.09% nitrogen, 20.95% oxygen, 0.93% argon, 0.033% carbon dioxide, and small amounts of other gases. Air also contains a variable amount of water vapor, on average around 1% and strongly varies locally. Regardless of their small absolute volumes, ozone, vaporised water and water play an important role in atmospheric optics, because of their strong absorption of ultraviolet and infrared, respectively. Additional importance is attached to water, because of its influence on the growth behavior of particles in the atmosphere, which has a big influence on particle sizes of hygroscopic nuclei.

However, the concentration of gases in the atmosphere is not constant. The atmosphere, that is to say the overall envelope of the earth is several hundred kilometers thick, gases and therefore optical characteristics alter greatly with altitude. Hence this work will restrict the altitude of interest to Troposphere that the layer directly above the ground

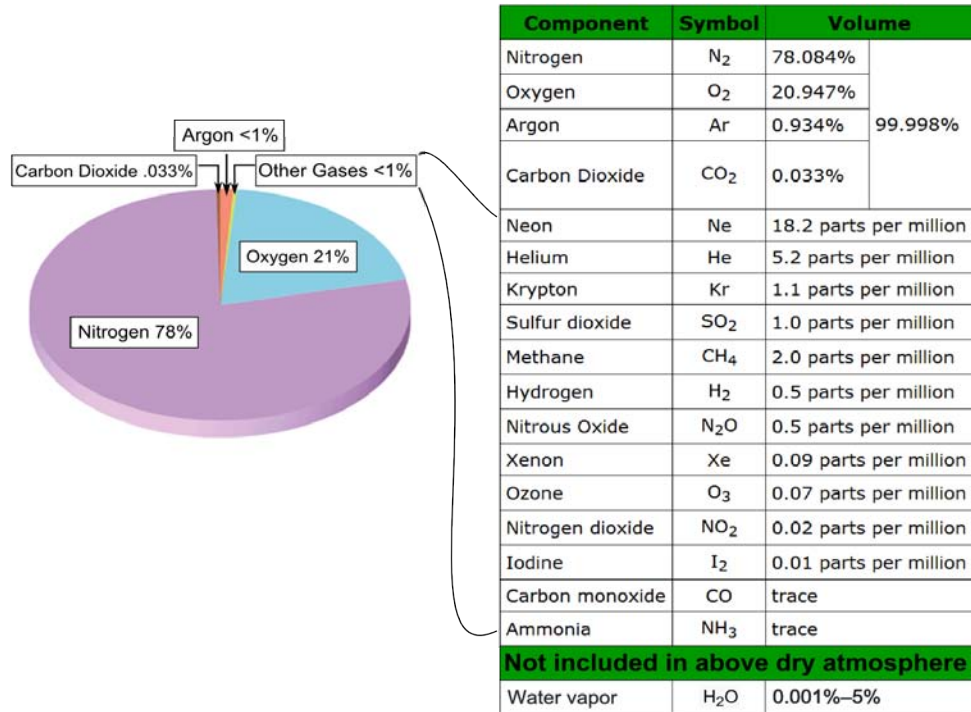


FIGURE 2.7: Major constituents of dry air, by volume

and just a few kilometers above in order to confine the work to just what is needed for the desired application of image dehazing near the ground.

Also, these are not the only particles present in the atmosphere, all types of particles responsible for atmospheric scattering are shown in table 2.1, more details referred Fig.2.8. Haze particle, fog droplet and cloud droplet are strong light-scatterers. This is mainly because their larger size that scatters light effectively, which will be dealt with later in this Chapter.

TABLE 2.1: Particles Responsible for Atmospheric Scattering

Type	Size(μm)	Concentration(cm^{-3})
Air molecule	10^{-4}	10^{19}
Aitken nucleus	$10^{-3} - 10^{-2}$	$10^4 - 10^2$
Haze particle ^a	$10^{-2} - 10$	$10^3 - 10$
Fog droplet	$1 - 10$	$100 - 10$
Cloud Droplet	$1 - 10$	$300 - 10$
Raindrop	$10^2 - 10^4$	$10^{-2} - 10^{-5}$

a:Including $PM_{2.5}$ and PM_{10}

Scattering of Light by small particles and molecules in the atmosphere

Different from reflection, where radiation is deflected in one direction, some particles and molecules found in the atmosphere have the ability to scatter solar radiation in all

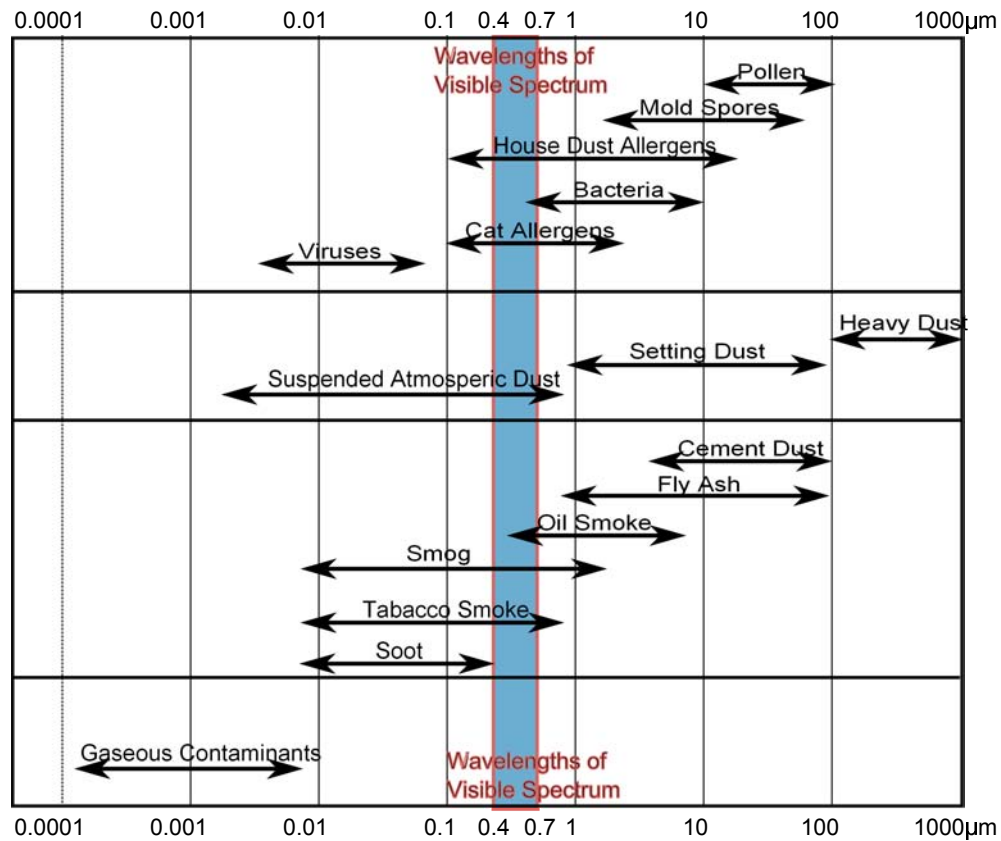


FIGURE 2.8: Airborne particulate size and wavelength of visible spectrum

directions Fig.2.9. The particles/molecules which scatter light are called scatterers and can also include particulates made by human industry.

The size of a scattering particle is often parameterized by the ratio

$$x = \frac{2\pi r}{\lambda} \quad (2.2)$$

where r is its characteristic length (radius) and λ is the wavelength of the light. Objects with $x \gg 1$ act as geometric shapes, scattering light according to their projected area. At the intermediate $x \simeq 1$ of Mie scattering, interference effects develop through phase variations over the object's surface. Rayleigh scattering applies to the case when the scattering particle is very small ($x \ll 1$, with $r < \lambda/10$ wavelength) and the whole surface re-radiates with the same phase.

2.3.2 Rayleigh scattering

Rayleigh scattering shown in Fig.2.10, named after the British physicist Lord Rayleigh [15], is the dominantly scattering of light or other electromagnetic radiation by particles

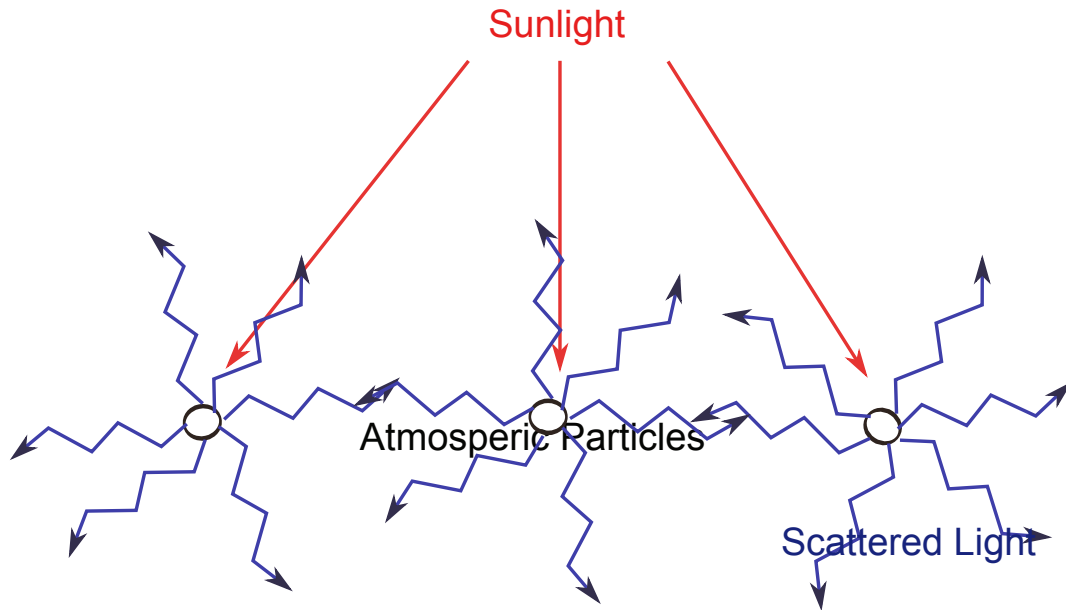


FIGURE 2.9: Scattering of Light by small particles and molecules in the atmosphere

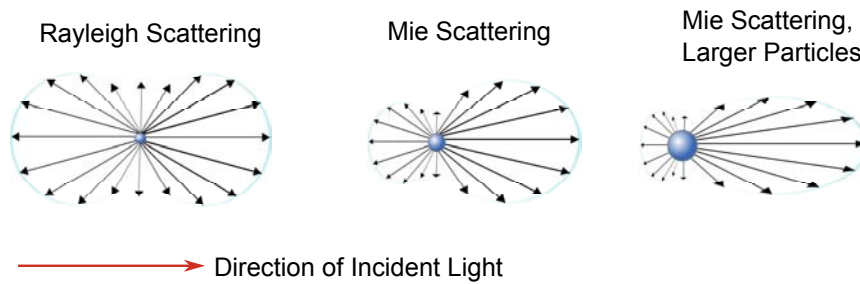


FIGURE 2.10: Mie scattering Compare with Rayleigh scattering

much smaller than the wavelength of the light.

In detail, the intensity I of light scattered by any one of the small spheres of diameter d and refractive index n from a beam of unpolarized light of wavelength λ and intensity I_0 is given by

$$I = I_0 \frac{1 + \cos^2 \theta}{2R^2} \left(\frac{2\pi}{\lambda} \right)^4 \left(\frac{n^2 - 1}{n^2 + 1} \right)^2 \left(\frac{d}{2} \right)^6 \quad (2.3)$$

The Raleigh phase function looks like this, according to [16]:

$$P(\theta) = \frac{3}{4}(1 + \cos^2 \theta) \quad (2.4)$$

where θ is the scattering angle between the incident beam and the scattered ray of light. An angle of 0 degrees means forward scattering along the direction of the incident beam. An angle of 180 degrees constitutes backward scattering. Averaging this over all angles gives the Rayleigh scattering cross-section[17],

$$\sigma_s = \frac{2\pi^5 d^6}{3 \lambda^4} \left(\frac{n^2 - 1}{n^2 + 1} \right)^2 \quad (2.5)$$

The fraction of light scattered by a group of scattering particles is the number of particles per unit volume N times the cross-section. It can be seen from the above equations that Rayleigh scattering is strongly dependent upon the size of the particle and the wavelengths. The intensity of the Rayleigh scattered radiation increases rapidly as the ratio of particle size to wavelength increases. Furthermore, the intensity of Rayleigh scattered radiation is identical in the forward and reverse directions.

2.3.3 Mie Scattering

The Rayleigh scattering model breaks down when the particle size becomes larger than around 10% of the wavelength of the incident radiation. In the case of particles with dimensions greater than this, Mie's scattering model [18] can be used to find the intensity of the scattered radiation. The intensity of Mie scattered radiation is given by the summation of an infinite series of terms rather than by a simple mathematical expression [19]. The phase function which models the scattering of light by Mie regime particles is approximated by the Henyey-Greenstein function which is as follows, according to [16]:

$$P(\theta) = \frac{1}{2} \frac{1 - g^2}{(1 + g^2 - 2g \cos \theta)^2} \quad (2.6)$$

Where the asymmetric parameter g is a parameter derived from the phase function and gives the relative direction of scattering by particles or gases.

It can be shown in Fig.2.10, however, that Mie scattering differs from Rayleigh scattering in several respects: it is roughly independent of wavelength and it is larger in the forward direction than in the reverse direction. The greater the particle size, the more of the light is scattered in the forward direction.

Mie scattering is not strongly wavelength dependent and produces the almost white glare around the sun when a lot of particulate material is present in the air. It also gives us the the white light from mist and fog.

2.4 Degradation Model

Light scattering occurs when light interacts with particles suspended in the air. Effects of scattering are felt daily as we perceive the sky to be blue or reddish, depending

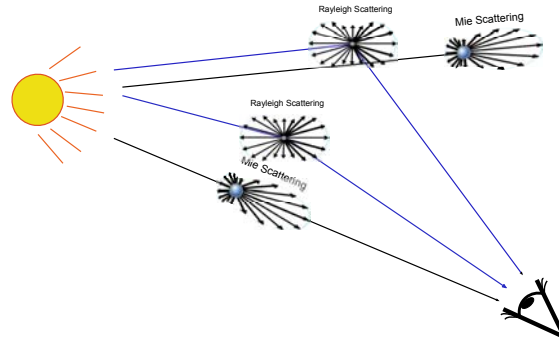


FIGURE 2.11: Rayleigh and Mie Scattering

on atmospheric conditions and solar illumination. Atmospheric scattering has been extensively studied by physicists and meteorologists. Light passing through a scattering medium is attenuated along its original course and is distributed to other directions. This process is commonly modeled mathematically by assuming that along short distances there is a linear relation between the fraction of light deflected and the distance traveled.

According to [15], if particles in the atmosphere are spherical or small, light is scattered symmetrically with respect to incident rays of light. We represent the portion of light that is scattered by a function $F(\lambda, \theta)$, the angular scattering function. The variable θ is the angle between the incident ray of light and the emanating ray of light; λ is the wavelength.

According to [20], atmospheric scattering manifest itself through two phenomena. The first phenomenon is attenuation of power; the second is sky intensity, we discuss separately.

2.4.1 Attenuation of power

Take a beam of light projected through a scattering medium, as illustrated in Fig. 2.12. The distance between object and observer is d . As rays of light are deflected by particles, the power of light conveyed by the beam decreases. For a differential portion of the trajectory, power decreases as $dP = -\beta(\lambda)Pdd$ [21], where $P_0(\lambda)$ is the power of the source and $\beta(\lambda)$ is called the *total extinction coefficient*, It represents the ability of the volume to scatter flux of a given wavelength in all directions. By integration through the whole path, the received power intensity is given by:

$$P(\lambda) = P_0(\lambda) \exp(-\beta(\lambda)d) \quad (2.7)$$

The intensity of an image shot by the observer is interested. Two factors affect the relationship between power and intensity. Power decreases with distance by the inverse square law so power decreases with d^2 , on the other hand, intensity at a receiver increase with square of distance d^2 , because the solid angle subtended by the receiver corresponds to a larger area on the object. [20] shows how the two effects cancel each other, so that the dependency of distance remains restricted to the exponential term. For an object with intensity $I_0(\lambda)$ in the absence of scattering and distance d from the viewer, the intensity measured by the viewer $I(\lambda)$ is:

$$I(\lambda) = I_0(\lambda) \exp(-\beta(\lambda)d) \quad (2.8)$$

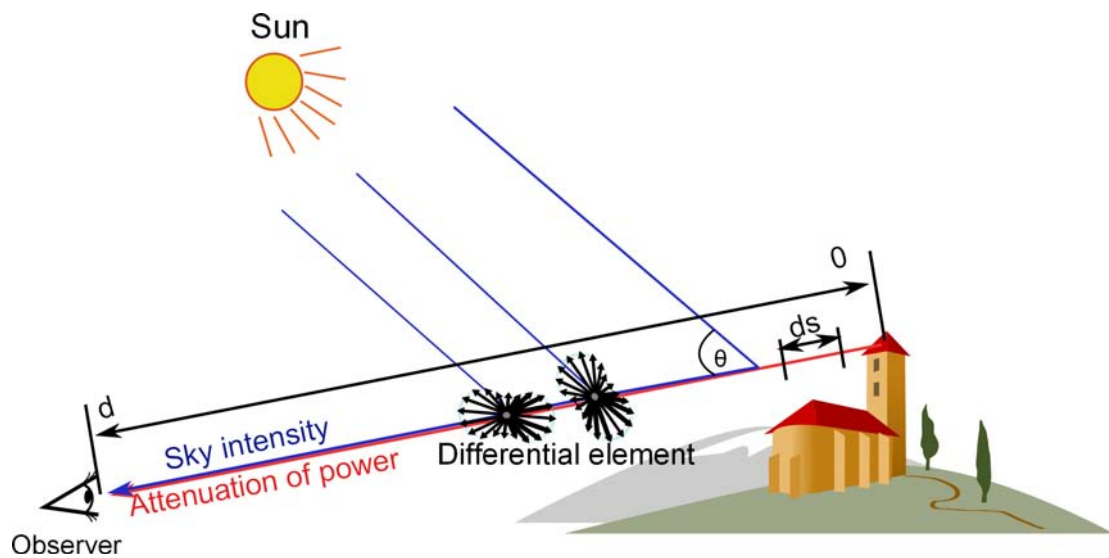


FIGURE 2.12: Light travels from an object to a observer through the air and sky intensity under uniform illumination(sunlight)

2.4.2 Sky intensity

Even though light power is attenuated by direct scattering, there is another effect, also due to scattering, which increase the power in a light beam.

Consider an imaginary line, traced from the observer to some point infinitely far away in a scattering medium. Suppose the line is illuminated by a uniform source from the top, for instance, the sky. At each point of the line, scattering events take place and divert light from its original path.

As light is directed to the observer from all points in the line, the observer perceives a new source of light, due exclusively to scattering.

From the previous sections, we suppose that the light coming from any point at distance x is affected by the angular scattering function and is attenuated exponentially. To obtain the amount of light received in this way, we assume

- *illumination from the sky is uniform and rays of light from sky are parallel*
- *Each ray of light is scattered once*

we integrate the effect of scattering events from the viewer to an arbitrary distance d [22]:

$$P'(\lambda) = \int_0^d P'_0(\lambda) F(\lambda, \theta) \exp(-\beta(\lambda)x) dx \quad (2.9)$$

which lead to:

$$P'(\lambda) = \frac{P'_0(\lambda) F(\lambda, \theta)}{\beta(\lambda)} (1 - \exp(-\beta(\lambda)d)) \quad (2.10)$$

Then we assume:

The variation of θ across an object located relatively far away is small enough so that its effect in $\frac{P'_0(\lambda) F(\lambda, \theta)}{\beta(\lambda)}$ is negligible.

Assuming that this added light is dominated by light that underwent multiple scattering events, allows us to approximate it as being both isotropic and uniform in space. This constant light $A(\lambda)$, known as the *airlight* [23] or also as the *veiling light*.

2.4.3 Combining scattering effects

According to [24], attenuation and sky intensity are additive due to the linear character of light propagation. Suppose an object located at distance d has intensity $I_0(\lambda)$ when imaged in a vacuum. In the presence of atmosphere the intensity is:

$$I(\lambda) = I_0(\lambda) \exp(-\beta(\lambda)d) + A(\lambda)(1 - \exp(-\beta(\lambda)d)) \quad (2.11)$$

In a non-polluted atmosphere, without rain or snow, scattering is mainly caused by small particles and is sensitive to λ , for instance, such particles produce an extinction coefficient that is larger for red and smaller for blue, which causes the sky to be blue and distant mountains to appear bluish. For d is not so large, there is no appreciable "blueing" effect. For larger particles, Mie scattering are dominate, the dependence on wavelength becomes negligible. Due to such considerations, we drop the dependency on

λ in the remainder of the thesis. Referring the measured intensity of an object as I , and the intensity of the object without scattering as J , we arrive at our basic equation:

$$I = J \exp(-\beta d) + A(1 - \exp(-\beta d)) \quad (2.12)$$

The 2.12 is called degraded fog model in some papers, in section 4.1 a haze model in RGB model will be introduced.

Chapter 3

Previous Work of Dehazing

During the past decade many researchers have been devoted on the problem of how to obtain high quality dehazed image [3] [4][5] [25] [20][26][27][28] [29] [30] [31][32] [33][34]. In this chapter, We will introduce and analyze the existing dehazing methods.

3.1 Overview of dehazing method

Many ways can lead to achieve the goal of haze removal and visibility improvement. The methods can basically be divided into three groups: non-model-based methods, model-based multi images or intervention-required methods, model-based single image methods. Fig.3.1 shows comparison of their representative methods and image processing effects, the images are taken from Fattal(2008) [5].

Those non-model-based methods trying to enhance the contrast of an image using simpler computer vision techniques such as gamma correction, histogram equalization or unsharp masking.

Representative model-based multi-image or intervention-required methods come from Schechner, et. al.(2003) [27], Narasimhan et al.[35], [36] and Kopf et al.(2008) [30]. Schechner, et. al.(2003)notice that the airlight scattered by atmospheric particles is partially polarized. Based on this observation, they develop a quick method to reduce hazes by using two images taken through a polarizer at different angles. Narasimhan et al. propose a physics-based scattering model [35] [36]. By this model, the scene structure can be recovered from two or more weather images. Kopf et al. [30]propose to dehaze an image by using the scene depth information directly accessible in the georeferenced digital terrain or city models.

Model-based single image dehazing, in contrast, is a more challenging problem, since fewer information about the scene structure is available. Recently, some significant advances have also been achieved [5], [4] [3] [37]. These progresses benefit much from the insightful explorations on new image models and priors. Fattal(2008) [5] proposes a refined image formation model to account for the surface shading and the scene transmission. Under the assumption that the two functions are locally statistically uncorrelated, a haze image can be broken into regions of constant albedo, from which the scene transmission can be inferred. Tan(2008) [4] proposes to enhance the visibility of a haze image by maximizing its local contrast. Following Tan(2008), Tarel et al.(2009) [38] points out visibility restoration is an ill-posed problem and a regularized solution can be obtained by maximizing the contrast of the resulting image assuming that the depth-map must be smooth except along edges with large depth jumps. The problem can thus be reformulated as maximizing atmospheric veil assuming than atmospheric veil is smooth most of the time, and formalized an optimization problem. By simplifying this optimization problem, the algorithm obtain a high processing speed. especially in regions with very dense hazes. However, since it is not a physics-based method, the restored image often suffers from distorted colors and significant halos. He et al.(2011)[3] present an interesting image prior - dark channel prior for single image dehazing subtraction from Chavez(1988)[25]. This prior comes from an observation that most local patches in haze-free images often contain some low intensity pixels. The prior, combined with a Guided image filtering operation [6], can achieve a quite compelling haze-free result of very high quality. Kratz et al.[37] model an image as a factorial Markov random field, in which the scene albedo and depth are two statistically independent latent layers. A canonical expectation maximization algorithm is implemented to factorize the image. Kratz's method can recover a haze-free image with fine edge details, but the results often tend to be over enhanced. More reference [39][40] [41] [42] [43] [44] [45] [46] [47] [48] [49].

Fig.3.1 shows comparison of their representative methods and image processing effects, some images are taken from Fattal(2008) [5]. Fig.3.1(a) shows the input image, Fig.3.1(c1) is the result of a polarisation based dehazer, due to its outstanding image quality this method can be seen as reference method. Fig.3.1(b1-3) contains images, whose visibility have been improved by simpler image processing methods such as gamma correction, histogram equalisation and unsharp masking, respectively. Fig.3.1(d1-3) contains the results of Fattal(2008), Chavez(1988) and He(2009). Fattal's results are the best for the single image dehazing methods in this comparison, He et al.(2009) produces comparable results to those of Fattal, which shows that single image model based, recently developed methods are the way to go. Also Tan(2008) [4] and Kopf et al.(2008) [30], Tarel et al.(2009) [38] respectively, are workers in this field with their own

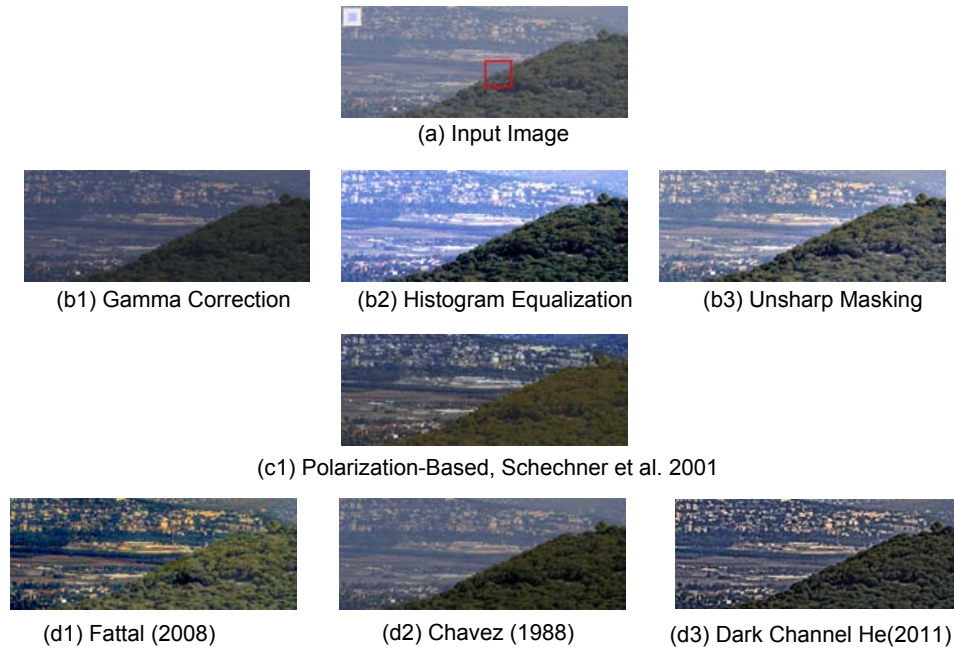


FIGURE 3.1: Comparison of computed images from the same input image created with different dehazing techniques.

image dehazing methods each. The methods of Tan(2008) [4] and Tarel et al.(2009) [38] Running fast. Kopf et al.(2008) [30] gives outstanding results, and is one of the best in quality available today. These five works are compared in the Fig.3.2, some images are from Tarel et al.(2009) [38].

3.2 Non-Model-Based dehazing method

The middle row in Fig.3.1(b1-3) shows the results of the non model based contrast enhancers. The striking similarity is the blue hue that the three have in common, this is the typical blueness of small haze particles as described in the preceding chapter. This can only be eliminated with model based techniques. These are just a few examples, there are actually many contrast manipulation algorithms available, mostly known from photography. It is considered humans have a minimum contrast threshold that is needed for object separation. Luckily, this contrast threshold can be raised in images using simple mathematical concepts like the gamma correction, unsharp masking or histogram equalisation. These were not developed to dehaze images, can however improve visibility for the human eye, hence they can also be used to further improve an already dehazed image. Thus for this purpose, they should not be used exclusively, but in combination with a dehazer. For the sake of completeness however, the three introduced concepts will now be described very briefly.

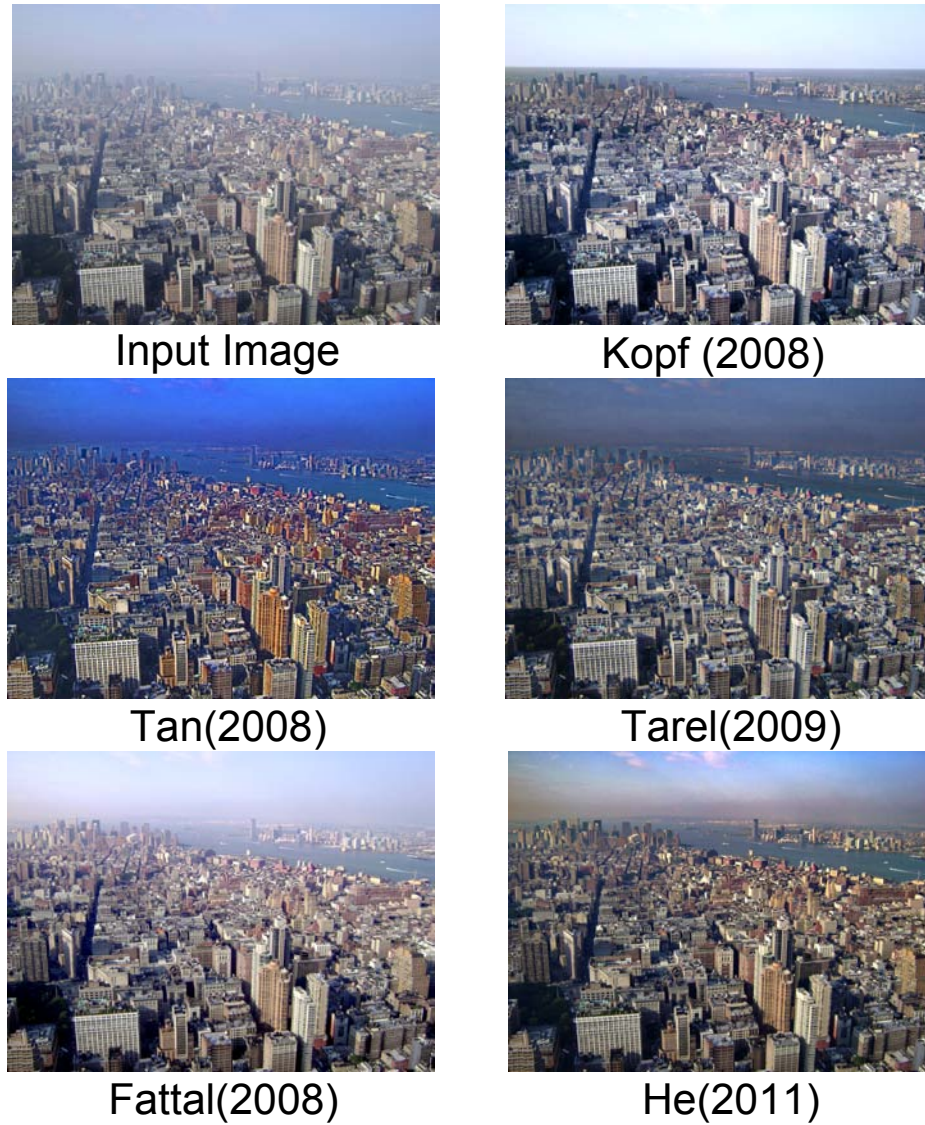


 FIGURE 3.2: Comparison of five Dehazing algorithm

3.2.1 Gamma Correction

Gamma correction, is the name of a nonlinear operation used to code and decode luminance or tristimulus values in video or still image systems [50]. Gamma correction is, in the simplest cases, defined by the following power-law expression:

$$V_{out} = AV_{in}^{\gamma} \quad (3.1)$$

where A is a constant and the input and output values are non-negative real values; in the common case of $A = 1$, inputs and outputs are typically in the range $0 - 1$. A gamma value $\gamma < 1$ is sometimes called an encoding gamma, and the process of encoding with this compressive power-law nonlinearity is called gamma compression; conversely

a gamma value $\gamma > 1$ is called a decoding gamma and the application of the expansive power-law nonlinearity is called gamma expansion.

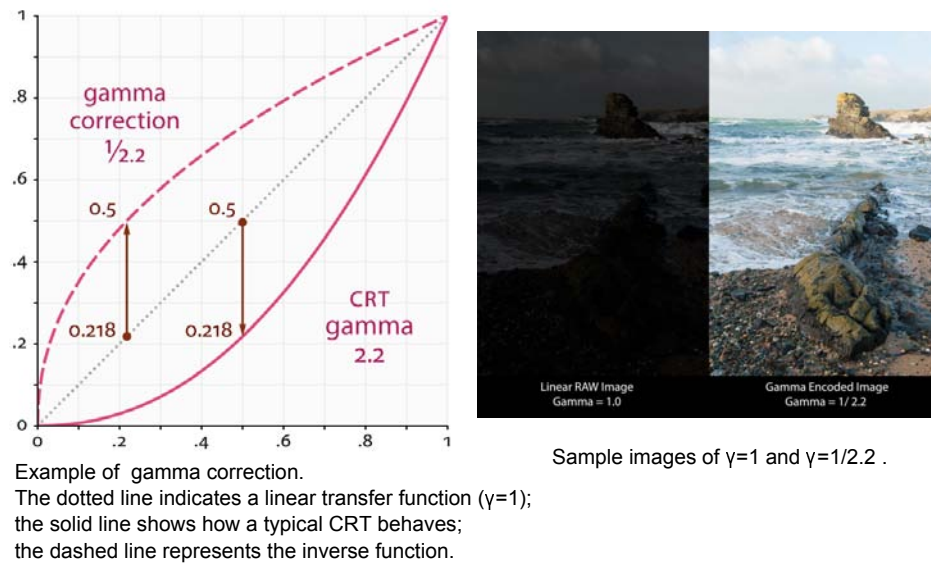


FIGURE 3.3: Plot shows the principle of gamma correction and sample images
 source:http://en.wikipedia.org/wiki/Gamma_correction
<http://www.wildlifeinpixels.net/blog/tag/tonal-distribution/>

Fig.3.3 shows the the principle of gamma correction, and sample images shows that when $\gamma < 1$ make dark regions lighter.

3.2.2 Histogram Equalisation

In general, a histogram is the estimation of the probability distribution of a particular type of data. An image histogram is a type of histogram which offers a graphical representation of the tonal distribution of the gray values in a digital image. By viewing the images histogram, we can analyze the frequency of appearance of the different gray levels contained in the image. In the right hand of Fig.3.3 we can see an image and its histogram. The histogram shows us that the image contains only a fraction of the total range of gray levels. In this case there are 256 gray levels and the image has higher probability of values between approximately 50 – 100. Therefore this image has low contrast.

A good histogram is that which covers all the possible values in the gray scale used. This type of histogram suggests that the image has good contrast and that details in the image may be observed more easily.

As stated earlier, basically the histogram equalization spreads out intensity values along the total range of values in order to achieve higher contrast. This method is especially

useful when an image is represented by close contrast values, such as images in which both the background and foreground are bright at the same time, or else both are dark at the same time. For example, the result of applying histogram equalization to the image is presented in the left hand of Fig.3.3. As we can clearly see from the images that the new image contrast has been enhanced and its histogram has also been equalized. There is also one important thing to be note here that during histogram equalization the overall shape of the histogram changes, where as in histogram stretching the overall shape of histogram remains same.

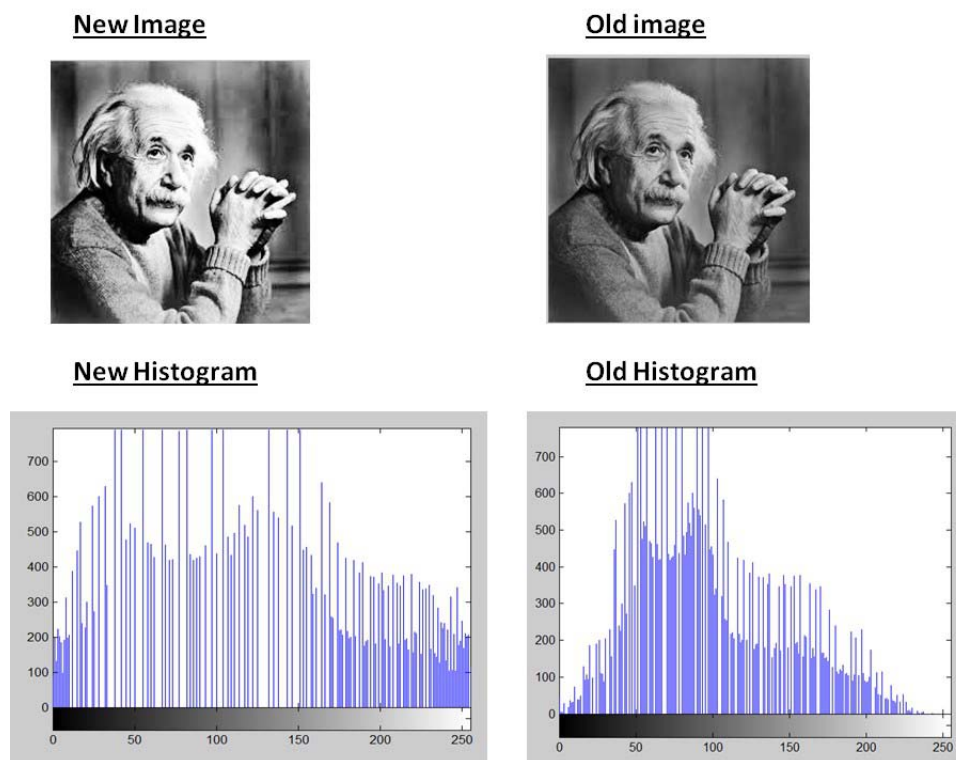


FIGURE 3.4: Comparison of both the histograms and images before histogram equalization and after.

source: http://www.tutorialspoint.com/dip/Histogram_Equalization.htm

A disadvantage of this method is that it may increase the noise by discriminating it from the actual usable signal. However, this method is one of the more advanced methods to improve image contrast, and is of the three mentioned in this thesis the most resource intensive, but usually also the one with the best results. This method generally improves the global contrast, locally however spots in the image with close brightness values may not be improved in some cases.

3.2.3 Unsharp Masking

Sharpness makes edges clear and distinct. Unsharp masking produces an edge image $g(x, y)$ from an input image $I(x, y)$ via

$$G(x, y) = I(x, y) - I_{smooth}(x, y) \quad (3.2)$$

where $I_{smooth}(x, y)$ is a smoothed version of $I(x, y)$. This edge image can be used for sharpening if we add it back into the original signal.

$$I_{sharp}(x, y) = I(x, y) + k * G(x, y) \quad (3.3)$$

where k is a scaling constant. Reasonable values for k vary between 0.2 and 0.7, with the larger values providing increasing amounts of sharpening. Fig.3.5 shows a Real-World Example to illustrate principle of unsharp masking. Unsharp masking can increase

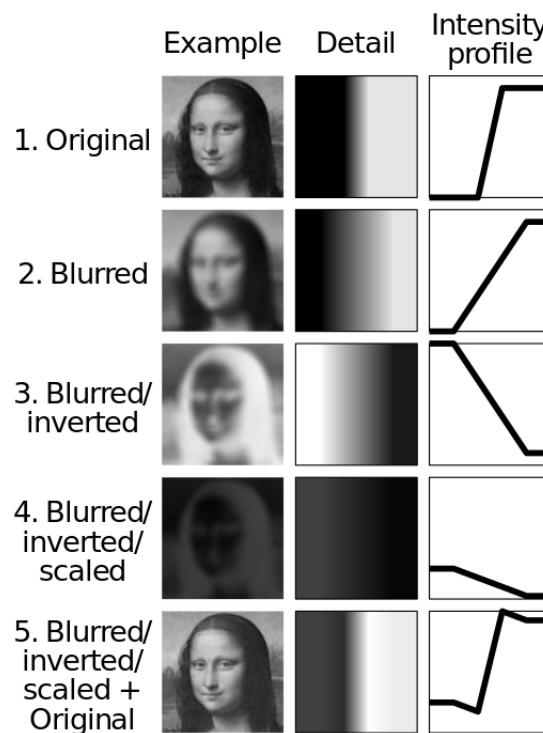


FIGURE 3.5: Simplified principle of unsharp masking
source: http://en.wikipedia.org/wiki/Unsharp_masking

either sharpness or local contrast because these are both forms of increasing differences between values, increasing slopesharpness referring to very small-scale (high-frequency) differences, and contrast referring to larger-scale (low-frequency) differences.

3.3 model-based multi-image or intervention-required dehazing methods

3.3.1 Visibility Improvement Based on Polarization Filtered Images

Polarisation-based dehazing methods are part of the multi-image or intervention-required group, they usually use two input images taken with two differently polarised filters, one after another, to produce one dehazed image. This technique makes use of the fact that the airlight is at least partially polarised, whereas the direct transmission of the object is unpolarised. Polarisation filters alone cannot eliminate haze in scenes, at least two images with different polarisation filter states are necessary. The assumed model is that of Koschmieders theory with additional polarisation filters, see Fig.3.6.

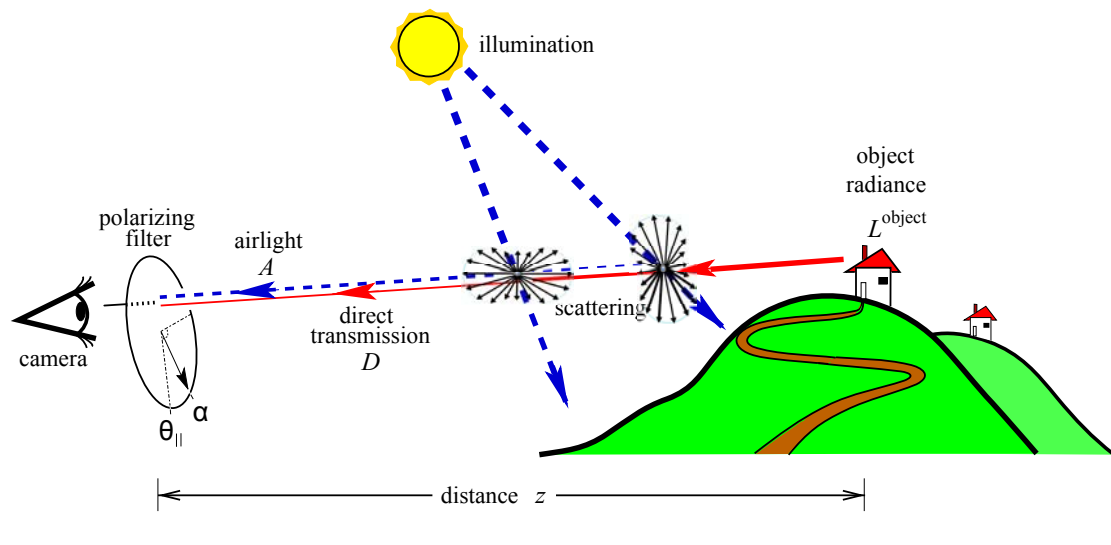


FIGURE 3.6: Model for polarisation-based dehazing.

With the knowledge from Fig.2.12, this figure is pretty much self-explanatory. In this section, the basic principles are described behind the method shown in [51], however this is also representative for all other known polarisation-based methods.

Consider Fig.3.6, the resulting image of a scene consists of two components, the first coming from the object radiance L^{object} and the second from the airlight A . The former is free of scattering in the line of sight and is only dependent on the attenuation of the atmosphere. The direct transmission $t(x)$ can then be written in:

$$t(x) = L^{object} \cdot \tau \quad (3.4)$$

where

$$\tau = \exp(-\beta d(x)) \quad (3.5)$$

is the transmittance of the atmosphere. Here $d(x)$ denotes the distance from the observer to the object and β the attenuation coefficient. The airlight, also called the path radiance, is produced by the scene illumination and given by:

$$A = A_\infty(1 - \tau) \quad (3.6)$$

Where A_∞ is the saturation airlight, which depends on the atmospheric and illumination conditions. It is the maximal possible intensity of airlight, which corresponds to the airlight of the sky near the horizon. In contrast to the direct transmission the airlight factor increases with distance and dominates the image irradiance I_{total} at long ranges:

$$I_{total} = t(x) + A \quad (3.7)$$

This is the major cause for reduction of image contrast in haze. The partially polarised airlight can now be used to restore a haze free image by mounting a polarisation filter with angle in the imaging system. When rotating the polariser, there is an orientation at which the image is least intense, let this be denoted by I_{min} . I_{min} corresponds to the lowest amount of airlight. This orientation of the polarisation filter may be denoted by θ_{\parallel} . When now rotating the pol. filter by 90° relative to θ_{\parallel} , then the image irradiance is strongest, since now the principle polarisation component of the airlight is strongest, this may be called I_{max} with θ_{\perp} . Once these two images are acquired, the dehazed image can be estimated by:

$$\hat{L}^{object} = \frac{I_{total} - \hat{A}}{\hat{\tau}} \quad (3.8)$$

where the estimated transmittance, $\hat{\tau}$ is :

$$\hat{\tau} = 1 - \frac{\hat{A}}{A_\infty} \quad (3.9)$$

and the estimated airlight \hat{A} is:

$$\hat{A} = \frac{I_{max} - I_{min}}{p} \quad (3.10)$$

Here p is the degree of polarisation of airlight, which depends on the particle size of the aerosols. It can however be estimated with just the parameters already known. It is measured from the raw images by looking at pixels which correspond to objects at infinity, naturally such pixels are those of the sky near the horizon (in later years,

Schechner et al. proposed ways to find p without having a horizon in the picture).

$$p = \frac{I_{max} - I_{min}}{I_{max} + I_{min}} \Big|_{d(x)=\infty} \quad (3.11)$$

Hence the airlight saturation value can be estimated from the same sky area as

$$p = [I_{max} + I_{min}]_{d(x)=\infty} \quad (3.12)$$

The distance map can be recovered as a byproduct:

$$\beta \hat{d}(x) = -\log \left[1 - \frac{\hat{A}}{A_\infty} \right] \quad (3.13)$$

This operation must be done for each color channel separately. The method works with only slight alterations for both atmospheric photography [27] as well as for underwater photography [32]. Problematic however, are surfaces that are specular, like windows or water, because they reflect partially polarised light and lead to errors in the calculation. These areas must be treated separately, and can for example be detected by analysing inconsistencies in the depth map, see Namer and Schechner(2005)[51]. Although this method is model based, no knowledge about the actual scattering particles is necessary. However, due to its basic principle, only Rayleigh scattering can properly be eliminated. Since Mie scatterers polarise the light in a different way if any(the larger the particle, the less the polarisation). Also clear day recording is preferred for this method, since then the airlight polarisation can properly be separated from the direct transmission. However, when the prerequisites are met, polarisation-based dehazing gives very good results, an example is given in Fig.3.7. Note that the correct colours can also be restored in contrast to the formerly mentioned enhancers that purely focus on the contrast without being model based.

Multi image dehazing methods in general, although usually giving qualitatively great results tend to be unsuitable for real-time image dehazing purposes. It is thinkable that for example, half the framerate could be sacrificed in order to capture two images with different polarisation state, however rotating a static polarisation filter is of course very slow when done by hand or even done by a clocked mechanical mechanism. Although there are now electronic liquid crystal based polarisation filters available on the market that may be able to switch on every frame, they are very colour selective and give different results for different wavelengths of light [51]. Namer and Schechner also stated, that: "While we still do not demonstrate dehazing in video, we currently assess the LC technology using still photography." [51]. Also there is the argument, that special hardware requirements may not be feasible in real world applications, since it may be

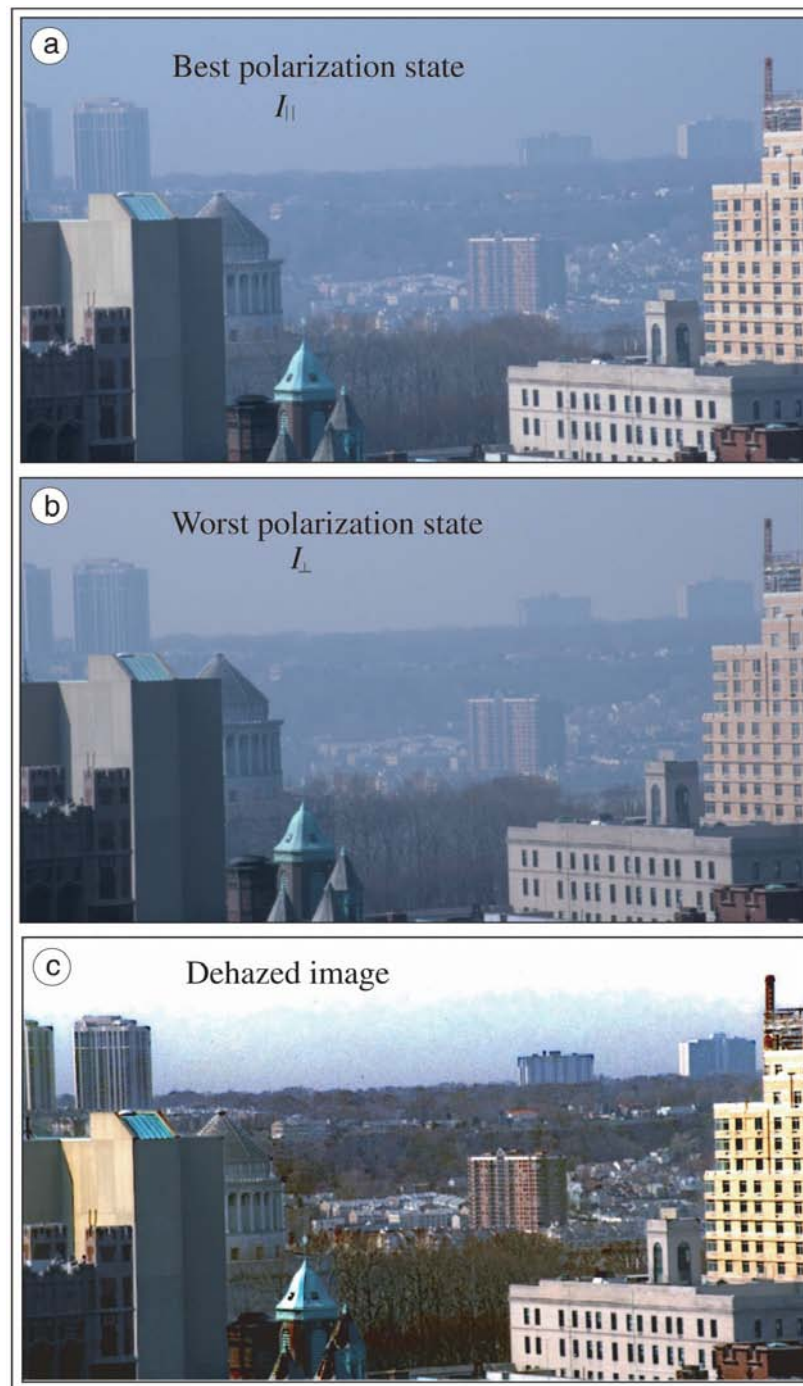


FIGURE 3.7: Example for polarisation-based dehazing, (a) shows the image taken with a polarisation filter under best polarisation state θ_{\parallel} (b) shows the image taken with a polarisation filter under worst polarisation state θ_{\perp} and (c) shows the dehazed image.

Source: Schechner, et. al.(2003)[27]

inconvenient in practice to equip once deployed cameras with a liquid crystal polarisation filter for simple physical or monetary reasons. Especially in windy weather conditions, cameras that are mounted on high masts and equipped with a polarisation filter may be very sensitive to translation. Thus two images of different polarisation state may be useless when shifted by a few pixels or even subpixels due to wind or other causes. Additionally to multi-image techniques, there are methods using multiple images such as the dehazing method of Nayar and Narasimhan described in [52] and [35], which require images taken under two different weather conditions. This is of course way too slow for real-time applications.

3.3.2 The Deep Photo System

A rather different approach was proposed by Kopf et al. in 2008 called the Deep Photo System. Crucial to all dehazing methods is to acquire the depth information of every pixel in the frame, but rather than acquiring these by making assumptions or employing statistical observations, Kopf et al. developed a data-driven dehazing procedure, by employing a registration process to align the photograph within an existing 3D model. This way the method does not need to estimate the distances in the scene, but will get the exact distances right away, assuming that such kind of georeferenced digital terrain and urban models are available. They propose a user interactive referencing system, in which the user registers certain scene points with the corresponding points in the model, such a model could come from satellite image data obtained from *GoogleEarthTM*, *BingMapsTM* or other providers. The 3D models for buildings and other objects are already available for many cities like Berlin or New York City and others (for example through *VirtualEarthTM*). Additionally helpful can be GPS tags, produced by the imaging system itself, sometimes even tilt and heading is provided by these cameras. With a static surveillance camera in mind, the scene must be georeferenced only once initially and could then rely on a set of depth information indefinitely assuming no camera shifts take place. Taking airports as an example, 3D models of buildings and high resolution geo information is usually available due to construction plans and air traffic controlling agencies. Here also lies the limitation of such a system, since it heavily relies on those sets of data, if no 3D model of the scene is available, no dehazing can be performed. Also in dynamic scenes, with vehicles such as aircrafts driving or flying through, there is no depth information for those foreground objects whatsoever, hence dehazing for those objects would rely on wrong depth information and cause a super-abundant dehazing on those spots. However, for scenes where distances are great and the influence of moving objects to scene distance is low, such as in Fig.??, the image quality is remarkable. After acquiring the depth information, the method of Kopf et al.

estimates the airlight and the attenuation coefficient similarly to the other haze removal methods and then basically solves Koschmieder's equation, however with some nuances differently. In the paper [30], the authors explore further possible applications for the depth information of an image, other than dehazing, such as approximating changes in lighting, expanding field of view, adding haze, adding new objects into the image with the correct haze values according to distance, and integration of GIS data into the photo browser, just to name a few. Since often the depth map of other dehazing methods also comes as a byproduct, these mentioned applications may also be implemented combined with other dehazers, such as [5] or [3], for example. Problems may arise from the fact that the alignment between the photograph and the model may not be completely accurate due to unprecise 3D models or the lens curvature of the imaging system.

3.4 model-based single image dehazing methods

3.4.1 Fattal's Method

Fattal introduced a new technique in 2008 for single image dehazing that produces qualitatively great results on hazy images. The main idea of this approach is to take the image degradation model from Rossum and Nieuwenhuizen ([22]) also known as the *Radiative Transport Equation* (shown in Eq.(3.14)) and express it in terms of surface shading in addition to the transmission. This gives a refined image formation model. Quoting Fattal: "This allows us to resolve ambiguities in the data by searching for a solution in which the resulting shading and transmission functions are locally statistically uncorrelated. A similar principle is used to estimate the color of the haze." [5].

$$I(x) = t(x)J(x) + (1 - t(x))A \quad (3.14)$$

In this equation, $t(x)$ is the transmission, a scalar for each colour component:

$$t(x) = \exp(-\beta d(x)) \quad (3.15)$$

Similar to the preceding section the term $t(x)J(x)$ is being called the direct attenuation and $(1 - t(x))A$ the airlight. Here $I(x)$ is the input image, $J(x)$ the haze free image and A the global atmospheric light colour vector. This equation is commonly used to describe the image formation in the presence of haze and was used before by, for example [25], [52] and [28]. This inherits many ambiguities in each pixel independently, such as in the airlight-albedo, that gives a large degree of freedom. Fattal however, manages to reduce

this degree: "To reduce the amount of this indeterminateness, we simplify the image locally by relating nearby pixels together." [5]. He does that by grouping pixels belonging to the same surface, thus having the same surface reflectance and therefore the same constant surface albedo. Now the key idea to resolve the airlight-albedo ambiguity is that he assumes that the surface shading l and the scene transmission t are statistically uncorrelated, because l depends on the illumination on the scene, surface reflectance properties and the scene geometry, whereas t depends on the density of the haze(

) and the scene depth. Fattal then presents an independent component analysis method to determine l and t . The same principle of uncorrelation is applied to the estimation of the airlight colour. This method also gives a depth map, which could be used over and over again for a static camera when using it in a real-time application. "The Method works quite well for haze, but has difficulty with scenes involving fog, as the magnitude of the surface reflectance is much smaller than that of the airlight when the fog is suitably thick." [53]. According to Fattal, the noise level in the input image influences the quality of the dehazed image greatly. However, with Fattal's method the absolute error in transmission and haze-free image are both less than 7% in tests where the real haze free image was known, explanatory: "In its essence this method solves a non-linear inverse problem and therefore its performance greatly depends on the quality of the input data." [5]. "Moreover, as the statistics is based on color information, it is invalid for grayscale images and difficult to handle dense haze which is often colorless and prone to noise." [3]. For examples of performance, please refer to Fig.3.2.

3.4.2 Tan's Method

Tan presented a single image based dehazing method in 2008, too. His proposed method is based on the optical model:

$$I(x) = L_{\infty}\rho(x) \exp(-\beta d(x)) + L_{\infty}(1 - \exp(-\beta d(x))) \quad (3.16)$$

with L_{∞} being the atmospheric light and $\rho(x)$ the reflectance, this formula is very similar to 2.12. The first term in this equation is the direction attenuation and the second term corresponds to the airlight A . He then expresses it in terms of light chromaticity and as a vector for the color components. In this formula are more unknowns than knowns. Nevertheless, there are some clues or observations that Tan makes use of in his algorithm:

1. "The output image, [...] must have better contrast compared to the input image I ." [4]
2. "The variation of the values of A [atmospheric light for the color components] is dependent solely on the depth of the objects, d , implying that objects with the same depth will have the same value of A , regardless their reflectance(ρ). Thus, the values of

A for neighbouring pixels tend to be the same. Moreover, in many situations A changes smoothly across small local areas. Exception is for pixels at depth discontinuities, whose number is relatively small.” [4]. 3. ”The input images that are plagued by bad weather are normally taken from outdoor natural scenes. Therefore, the correct values of [the direct attenuation] must follow the characteristics of clear-day natural images.” [4]. The author of this paper then proposes an algorithm employing the clues above. With \mathbf{I} being the input image, the algorithm is:

1. Estimate L_∞
2. Compute α (light chromaticity) from L_∞
3. Remove the illumination colour of \mathbf{I}
4. Compute the data term $\phi(p_x | A_X)$ from \mathbf{I}
5. Compute the smoothness term $\psi(A_x, A_y)$
6. Do the interference, which yields the airlight, A
7. Return the direct attenuation, $\mathbf{D}_{\gamma'}$, computed from A .

He also proposed a data cost function for step 4 in the framework of Markov random fields, which can be efficiently optimised by various techniques, such as graph-cuts. This algorithm is applicable for both colour and gray images. However, it does not recover the scenes original colour [4]. Despite its neat approach, this method is not easily applicable to real-time applications since it takes ”The computational time for 600×400 images, using double processors of Pentium 4 and 1 GB memory, approximately five to seven minutes (applying graph-cuts with multiple labels)” [4]. Also, this method has some flaws compared to other methods of for example Fattal and Kopf et al. in terms of image quality. Since it produces halos near depth discontinuities and ”The method tends to produce over enhanced images in practice.” [53]. As an example for Tans method in terms of image quality, please refer to Fig.3.2.

3.4.3 Dark Channel Prior

The success of recently developed techniques such as [5], [30] and [38] compared to earlier dehazing methods lies in using stronger assumptions. A very promising new single image technology, developed in 2010 called the Dark Channel Prior comes from He, Sun and Tang. This method does not rely on significant variance on transmission or surface shading in the input image and the output image is less effected by halos than

in [4]. Although every assumption limits the algorithm to specific use cases, the main assumption here seems to work for most outdoor scenes, except for those where "the scene object is inherently similar to the airlight over a large location and no shadow is cast on the object" [3]. The main prior in this method is, as the name lets assume, the dark channel prior, which is a statistical based assumption of haze-free outdoor images. The prior says, that in most of the local regions that are not sky, very often some pixels have a very low intensity in at least one of its colour channels(RGB). In the hazy image then, these dark pixels can be used to determine the true airlight, since the airlight is apparent on a dark object(as stated in the preceding chapter). The dark channel J^{dark} of J (the haze-free image) is defined as:

$$J^{dark}(x) = \min_{n \in \{r,g,b\}} \left(\min_{x \in \Omega(x)} (J^n(x)) \right) \quad (3.17)$$

where J^n is a colour channel of J and $\Omega(x)$ is a local patch centered at x . This statistical observation is called the *dark channel prior*. These low intensities come from natural phenomena such as shadows or just really dark or colourful surfaces. Since J^{dark} tends to be zero and as A^n , the corresponding channel of the atmospheric light is always positive, it may be written:

$$J^{dark}(x) = \min_{n \in \{r,g,b\}} \left(\min_{x \in \Omega(x)} \frac{(J^n(x))}{A^n} \right) = 0 \quad (3.18)$$

This can be used to estimate the transmission for that patch $\Omega(x)$ by putting Eq.(3.18) into the image formation model Eq.(3.13), however now in combination with the min operator:

$$\min_{n \in \{r,g,b\}} \left(\min_{x \in \Omega(x)} (I^n(x)) \right) = \tilde{t}(x) \min_{n \in \{r,g,b\}} \left(\min_{x \in \Omega(x)} (J^n(x)) \right) + (1 - \tilde{t}(x))A^n \quad (3.19)$$

with $\tilde{t}(x)$ denoting the transmission in a local patch, then putting Eq.(3.18) into Eq.(3.19) leads to:

$$\tilde{t}(x) = 1 - \min_{n \in \{r,g,b\}} \left(\min_{x \in \Omega(x)} \frac{J^n(x)}{A^n} \right) \quad (3.20)$$

which is a direct estimation of the transmission for each local patch. They then apply a soft matting algorithm on the depth map, this leads to a much smoother and detailed depth map. Having the transmission or depth map, the scene radiance according to Eq.(3.14) can now be recovered. However, since the direct attenuation term $J(x)t(x)$ can be very close to zero, the transmission is restricted to a lower bound t_0 for example $t_0 = 0.1$, since the scene radiance is typically not as bright as the atmospheric light A . The final scene radiance $J(x)$ may then be recovered by:

$$J(x) = \frac{I(x) - A}{\max(t(x), t_0)} + A \quad (3.21)$$

In the above calculations, the atmospheric light A was considered to be known, which is of course not the case, at least initially. Unlike other workers in the field, He et al. do not take the pixel with the highest intensity as the atmospheric light, since this could as well be a white surface such as a white car or a bright building veneer or artificial light source. He et al. pick the top 0.1% brightest pixels in the dark channel($\min_n(I^n)$), since these must be the most haze-opaque. Among these pixels, the pixel with the highest intensity in the input I is picked as the atmospheric light A . This may not be the brightest pixel in the image, but is more robust than the "brightest pixel" method according to [3]. This method seems very elegant and shows very good results, as one can see from Fig.3.2.

Chapter 4

Detecting Foggy Images and Estimating the Haze Degree Factor

At present, most outdoor video-surveillance, driver-assistance and optical remote sensing systems have been designed to work under good visibility and weather conditions. Poor visibility often occurs in foggy or hazy weather conditions and can strongly influence the accuracy or even the general functionality of such vision systems. Consequently, it is important to import actual weather-condition data to the appropriate processing mode. Recently, significant progress has been made in haze removal from a single image [5], [3], [4]. Based on the hazy weather classification, specialized approaches, such as a dehazing process, can be employed to improve recognition. Fig.4.1 shows a sample processing flow of our dehazing program.

Despite its remarkable value, determining weather information from a single image has not been thoroughly studied. Traditional algorithms are designed for specific applications or require human intervention. Weather-recognition systems for vehicles which depend on vehicle-specific priors, have been proposed [54], [55], [56]. Another proposed system [57] can automatically label images with high confidence by assigning weather labels, such as sunny, or cloudy; however, manual input constraints are required.

Against this background, the main aim of the current study is to develop a set of stable algorithms for the detecting foggy images and labeling the haze degree of images by using a factor with universal applications. In this paper, we propose a haze degree estimation function to automatically distinguish foggy images and label images with their corresponding haze degrees. We relied on the atmospheric scattering model analysis

and statistics derived from various outdoor images in order to develop the estimation function.

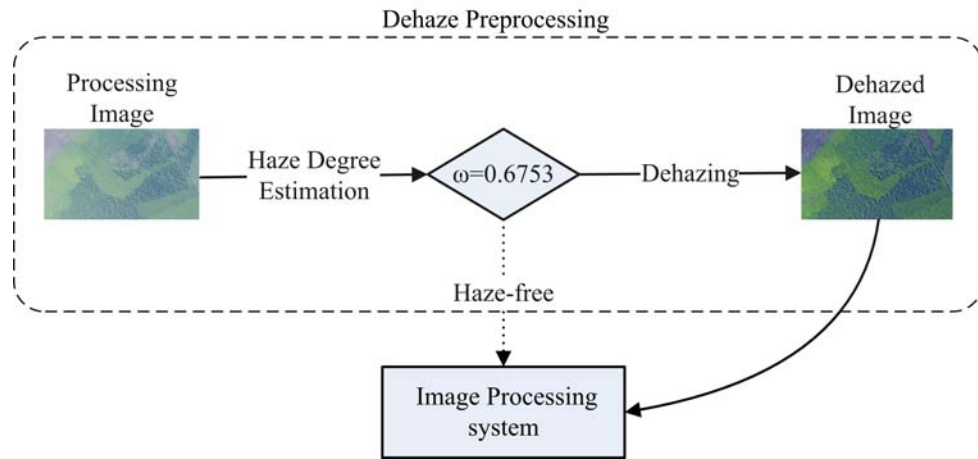


FIGURE 4.1: Sample dehazing flows by using haze degree estimation, where ω is a haze factor we defined

4.1 Atmospheric Scattering Model Analysis

By default, we discuss the case of image that use the RGB color model. A hazy image can be modeled as shown in [3], [35], (see Fig.4.2):

$$\mathbf{I}(\mathbf{x}) = \mathbf{J}(\mathbf{x})t(\mathbf{x}) + \mathbf{A}(1 - t(\mathbf{x})), \quad (4.1)$$

where \mathbf{x} denotes the pixel location, $\mathbf{I}(\mathbf{x})$ is the observed hazy image, and $\mathbf{J}(\mathbf{x})$ is the haze-free image. For $n \in \{r, g, b\}$, $\mathbf{I}^n(\mathbf{x})$ is one of three color channels of $\mathbf{I}(\mathbf{x})$, and $\mathbf{J}^n(\mathbf{x})$ is one of three color channels of $\mathbf{J}(\mathbf{x})$. \mathbf{A} is the global atmosphere light and is generally a fixed element A_0 in all three color channels, $\mathbf{A}^n = A_0$. $t(\mathbf{x})$ is the medium transmission and it is supposed to be the same in all three color channels at one pixel location. When the atmosphere is homogeneous, $t(\mathbf{x}) = \exp(-\beta \cdot \text{dep}(\mathbf{x}))$. Here, β is the scattering coefficient of the atmosphere, and $\text{dep}(\mathbf{x})$ is the scene depth. To determine the haze degree of an image rapidly and reliably, we define the following:

$$\mathbf{d}^{\mathbf{I}}(\mathbf{x}) = \min_{n \in \{r, g, b\}} \mathbf{I}^n(\mathbf{x}), \quad (4.2)$$

$$\mathbf{b}^{\mathbf{I}}(\mathbf{x}) = \max_{n \in \{r, g, b\}} \mathbf{I}^n(\mathbf{x}), \quad (4.3)$$

$$\mathbf{c}^{\mathbf{I}}(\mathbf{x}) = \mathbf{b}^{\mathbf{I}}(\mathbf{x}) - \mathbf{d}^{\mathbf{I}}(\mathbf{x}), \quad (4.4)$$

$$d = \frac{\sum_{\mathbf{x} \in \mathbf{x}} \mathbf{d}^{\mathbf{I}}(\mathbf{x})}{|\mathbf{S}_x \times \mathbf{S}_y|}, \quad b = \frac{\sum_{\mathbf{x} \in \mathbf{x}} \mathbf{b}^{\mathbf{I}}(\mathbf{x})}{|\mathbf{S}_x \times \mathbf{S}_y|}, \quad (4.5)$$

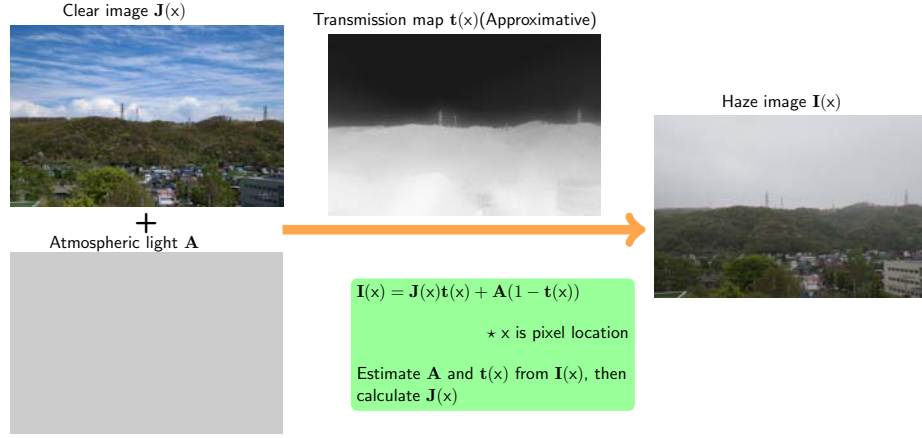


FIGURE 4.2: Atmospheric Scattering model used

$$c = d - b, \quad (4.6)$$

where $\mathbf{d}(x)$ is the minimum value of three channels, and $\mathbf{b}(x)$ is the maximum value. d and c , which are the average values of $\mathbf{d}^I(x)$ and $\mathbf{c}^I(x)$, are referred to as the dark and contrast values, respectively. Here, we assume that the size of image \mathbf{I} is $|\mathbf{S}_x \times \mathbf{S}_y|$. Take the minimum and maximum of the three channels on both sides of Eq.(4.1):

$$\begin{aligned} \mathbf{d}^I(x) &= \left(\min_{n \in \{r,g,b\}} \mathbf{J}^n(x) \right) t(x) + \mathbf{A}_0(1 - t(x)) \\ &= \mathbf{d}^J(x)t(x) + \mathbf{A}_0(1 - t(x)), \end{aligned} \quad (4.7)$$

$$\begin{aligned} \mathbf{b}^I(x) &= \left(\max_{n \in \{r,g,b\}} \mathbf{J}^n(x) \right) t(x) + \mathbf{A}_0(1 - t(x)) \\ &= \mathbf{b}^J(x)t(x) + \mathbf{A}_0(1 - t(x)), \end{aligned} \quad (4.8)$$

$$\mathbf{A}_0 - \mathbf{d}^I(x) = (\mathbf{A}_0 - \mathbf{d}^J(x))t(x). \quad (4.9)$$

By Eq.(4.8)-Eq.(4.7), we get the following

$$\begin{aligned} \mathbf{c}^I(x) &= \left(\max_{n \in \{r,g,b\}} \mathbf{J}^n(x) - \min_{n \in \{r,g,b\}} \mathbf{J}^n(x) \right) t(x) \\ &= (\mathbf{b}^J(x) - \mathbf{d}^J(x)) t(x) \\ &= \mathbf{c}^J(x)t(x). \end{aligned} \quad (4.10)$$

For most haze-free outdoor images, $\mathbf{d}^J(x) < \mathbf{A}_0$ even $\mathbf{d}^J(x) \ll \mathbf{A}_0$, Eq.(4.9) and Eq.(4.10) show that the smaller $t(x)$, $\mathbf{c}^I(x)$ and $\mathbf{A}_0 - \mathbf{d}^I(x)$ are closer to 0. As above, the values d and c may be correlated with the overall haze degree of an image. In the next section, we use a statistical method to evaluate the relationships.

TABLE 4.1: Standards dividing images into six groups

Haze-degree	Corresponding $\bar{\omega}$	Standards	
		Haze area proportion	Haze density
0	0.1	0	clear
1	0.3	0 – 80%	thin
2	0.5	0 – 80%	normal or thick
3	0.7	80% – 100%	thin
4	0.8	80% – 100%	normal
5	0.9	80% – 100%	thick

Note that, for simplicity, we estimate \mathbf{A} as follows. Clearly, $b \leq A_0 \leq \max_{\mathbf{x} \in \mathbf{x}} \mathbf{b}^{\mathbf{I}}(\mathbf{x})$ is established, and then, A_0 can be expressed as

$$A_0 = \lambda \max_{\mathbf{x} \in \mathbf{x}} \mathbf{b}^{\mathbf{I}}(\mathbf{x}) + (1 - \lambda)b, 0 \leq \lambda \leq 1. \quad (4.11)$$

Here, we set $\lambda = 1/3$.

4.2 Haze Degree Estimation Function

We selected 300 outdoor images that use the RGB color model (component values are stored as integer numbers in the range 0 - 255) and manually divided them into six groups according to the standards in Tab.4.1. Fig.4.3 shows the sample images from the six groups. A grade from 0 to 5 representing the haze degree is assigned to each group; the higher the grade, the hazier the image. Fig.4.4 shows the values of $(A_0 - d)$ (horizontal axis) and c (vertical axis) of images from six groups and the haze degrees of all selected images. The point colors represent the groups, and the point size indicates the haze degree, i.e., the larger points indicate greater haziness. It is evident that for most images from groups 3 to 5, $(A_0 - d)$ is less than 75 and c is less than 50. For most haze-free images (group 0, the smallest blue points), $(A_0 - d)$ is greater than 100 and c is larger than that in other groups.

To limit $\omega \in (0, 1)$, we introduce the following to estimate the haze factor ω :

$$\omega = \exp \left\{ -\frac{1}{2} (\mu x_1 + \nu x_2) + \sigma \right\}, x_1 = \frac{A_0 - d}{A_0}, x_2 = \frac{c}{A_0} \quad (4.12)$$

Obviously, $\ln(\omega)$ is a linear function of x_1, x_2 and σ . Each haze-degree were assigned a $\bar{\omega}$ in Tab.4.1. Using multiple linear regression analysis on our data set $\{\ln(\bar{\omega}_i), x_{i1}, x_{i2}\}_{i=1}^{300}$, we can get raw μ, ν and σ . Because μ, ν, σ are experience constants, we recommend $\mu = 5.1, \nu = 2.9, \sigma = 0.2461$.

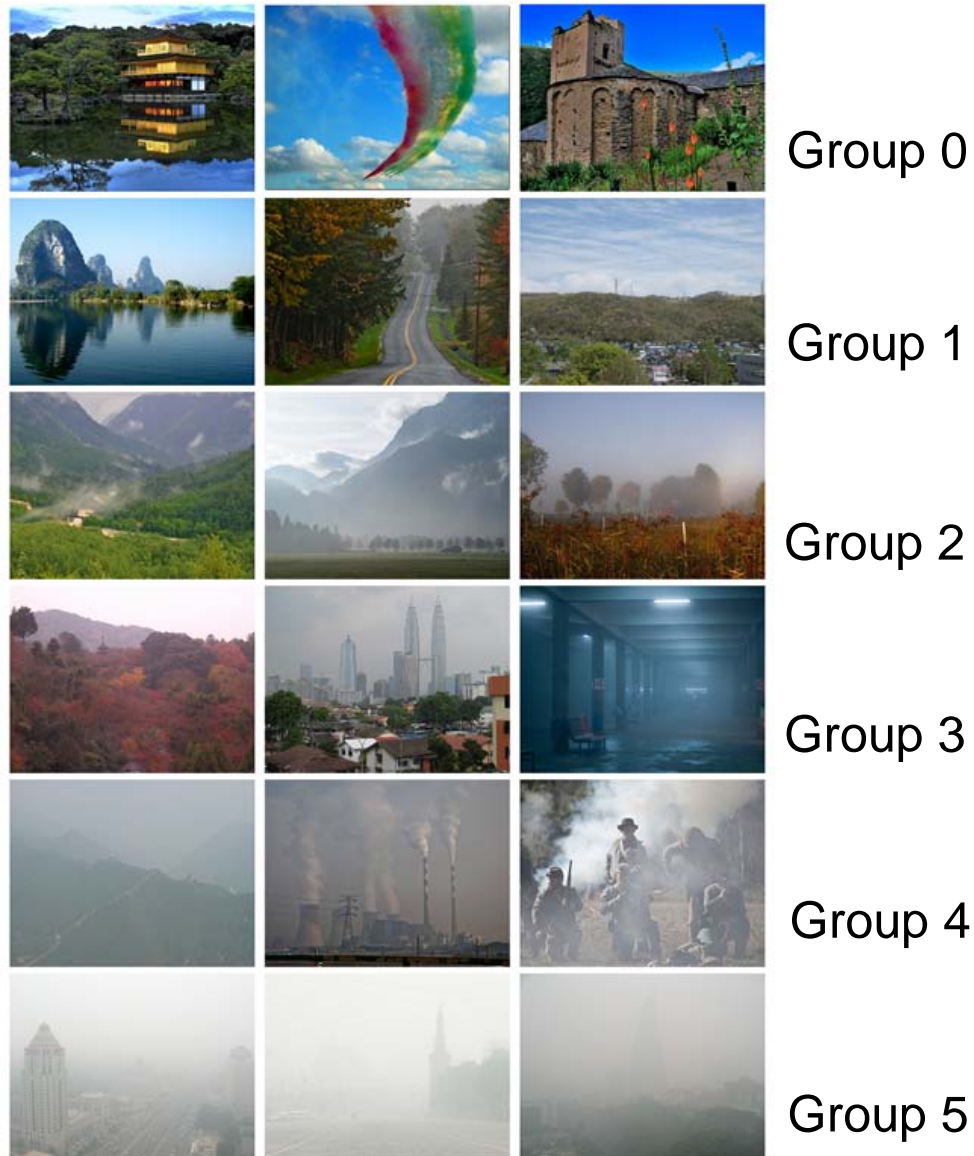

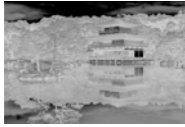



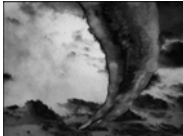




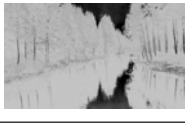
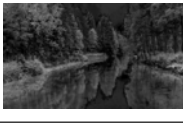

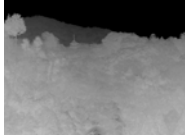












FIGURE 4.3: Sample images from our database

The main process of our algorithm is as follows:

1. Input processing image $\mathbf{I}(x)$.
2. Obtain $\mathbf{b}^{\mathbf{I}(x)}$, $\mathbf{d}^{\mathbf{I}(x)}$, $\mathbf{c}^{\mathbf{I}(x)}$ from $\mathbf{I}(x)$.
3. Calculate d, b, c , estimate the air light \mathbf{A}
4. Get haze factor ω by using Eq.(4.12).

TABLE 4.2: Haze-free sample images which have larger $A_0 - d$ and c and haze samples have smaller ones.

Image No.	Original image	$A - d(x)$	$c(x)$	$A_0 - d$	c
1				143.1593	45.5548
2				143.7508	96.16
3				168.209	87.2932
4				169.4447	54.8168
5				104.049	24.472
6				99.316	7.18002
7				74.148	8.14979
8				57.624	4.78021

4.3 Experimental Results

We used the Foggy Road Image Database(FRIDA) [58] to test the haze factor estimation function Eq.(4.5). FRIDA is comprised of 90 synthetic images of 18 urban road scenes. Each image is 640×480 pixels. (Mean execution time is 230 ms on an Intel Core I7 CPU.) Each image without fog (Lima set) is associated with four foggy images. Different types of fog are added to each of the four associated images: uniform fog(U080), heterogeneous fog(K080), cloudy fog(L080), and cloudy heterogeneous fog(M080), as an example Fig.?? shows the No.1 and No.10 images from five sets of FRIDA.

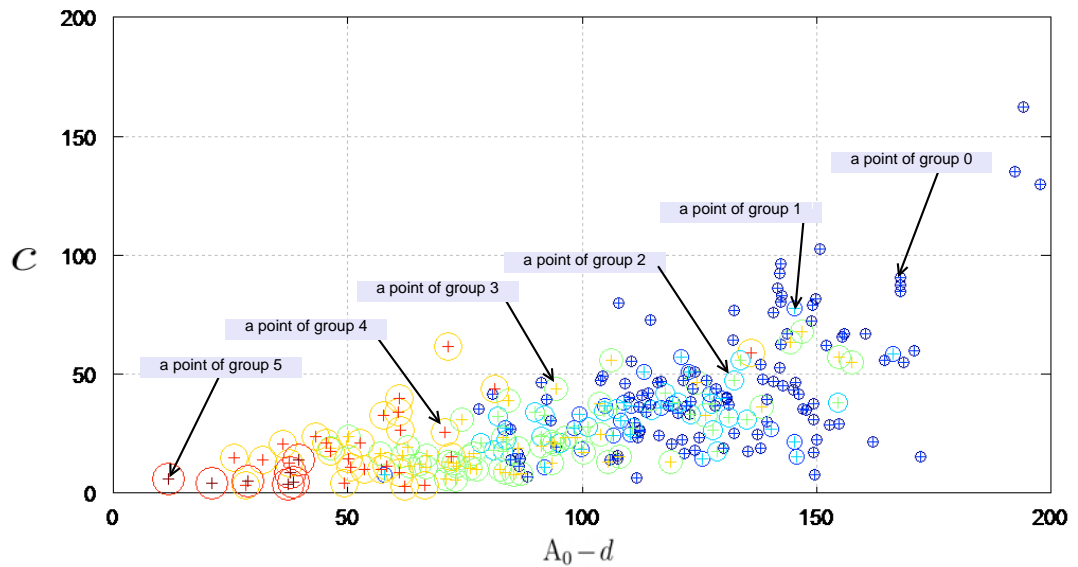


FIGURE 4.4: $A_0 - d$ (horizontal axis) and c (vertical axis) of images from six groups. Larger points correspond to higher haze grades.

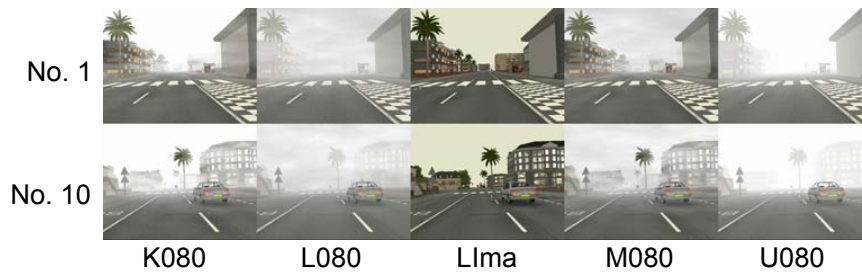


FIGURE 4.5: Sample images from FRIDA Database

As Fig.4.6 shows, the lowest haze degree (between 0.4 to 0.6) is found for images of Lima. Note that the sky area of images from the Lima set, is different from a real situation. Real fog-free image in our experimental results, have a degree of below 0.3. The four associated foggy images have regularity values (between 0.6 and 1) that correspond to different types of fogs. Images from U080 set always get the highest degree and M080 always get the lowest. For different images in the same set, for instance, No. 1 and No. 10, No. 10 gets higher degree than No. 1, which is consistent with the actual situation. The experimental results show that Eq.(4.12) can accurately distinguish haze degree.

In addition, we also randomly collected 48 real images to test our method dividing them by artificially picking three groups: haze-free, haze, and thick-haze. Fig.4.7 shows the haze factors of three groups and provides some sample images and the factor value. About 94% haze-free images get a haze-factor value below 0.4, 88% haze images get a value between 0.4 and 0.6, and, 85% thick images get a value between 0.7 and 1. Note that photo in the red circle, has haze-factor below 0.1, despite being a thick-haze airport

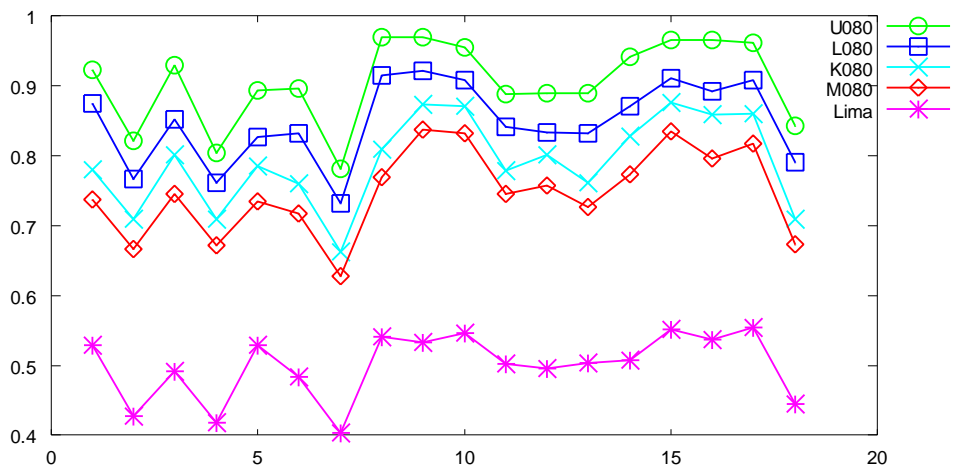


FIGURE 4.6: Estimated haze factor ω of the five sets of FRIDA, the horizontal axis is Image No. (1 - 18) and the vertical axis is the haze-factor ω .

night view obviously, this is because this picture has a monochrome light source, which means that \mathbf{A} was not the same in three channels which make our model fail.

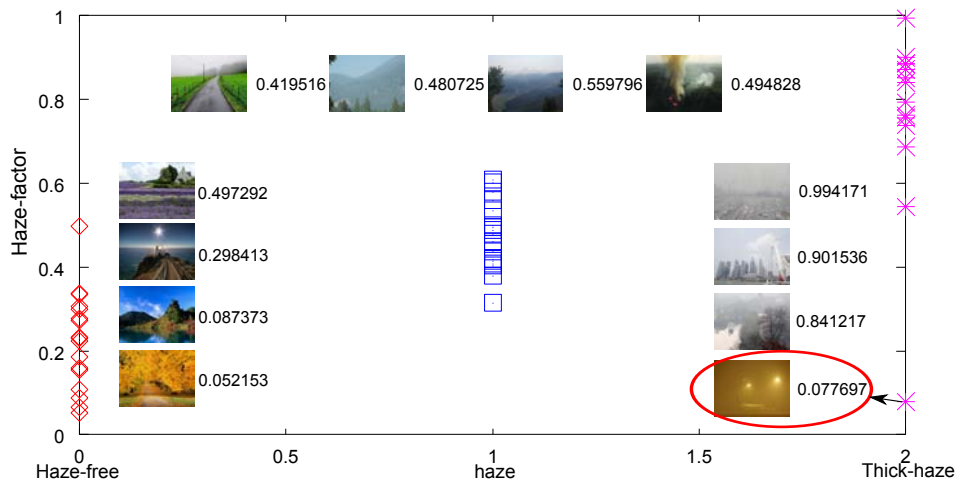


FIGURE 4.7: Estimated haze factor ω of real images divided in three groups and their sample images with the haze factor on the right.

4.4 Conclusions

We introduced a numerical foggy image detecting method by using the atmospheric scattering model analysis and statistics of various outdoor images, which can estimate the haze-factor from single image by using an adjustable empirical function without manual input constraint. Because its complexity is linear, it can be applied as an initial classification step of dehazing processing and does not exhaust processing resources.

Experimental results show that the method, can be applied to usual weather conditions in video-surveillance, driver-assistance and optical remote sensing system with high accuracy.

Our proposed prior is inspired by the atmospheric scattering mode, and suppose that the air light is equal in all three channels which might not always be true. Moreover, our method can-not be applied to the case of a monochrome light source. Thus we leave these problems for further research.

Chapter 5

Self-adjusting and Real-time Dehazing

Many outdoor computer vision applications like video surveillance, object detection, object recognition, tracking, intelligent vehicles and remote sensing systems etc. , assume that the input images have clear visibility. Unfortunately, this is not always true in many situations. Outdoor images or videos are usually degraded by light scattering and absorbing from the aerosols, such as dust, mist, and fumes in the atmosphere, here regarded as haze. the captured scenes suffer from poor visibility, low contrast, dimmed brightness and distorted color. therefore visibility improvement, contrast enhancement and features enhancement of images and videos captured in bad weather, also called as dehazing, is an inevitable task. In real-time dehazing, there are three problems to be solved: natural transition between frames, dehazing effect and processing speed. This paper proposes a simple and fast hazed degree Estimate method which is based on two basic observations: clear-day images have more contrast than images plagued by bad weather; in most of the local regions even the sky, hazed images have larger minimum values of most color(RGB)channel pixels closing to airlight value. Relying on these two observations, we develop an estimate function related to haze removal constant parameter ω . In order to reduce the computational cost while providing the promising dehazed results also for real-time applications, by modifying the dark channel prior, the transmission estimation is carried out by obtaining the minimum value from only the relevant pixel itself or the median filter of minimum values of its neighboring pixels. Experiments demonstrate that our results achieve good visibility and real-time computation.

5.1 Estimating the Transmission and Recovering the Scene Radiance

From the time analysis, most method based on Dark Channel Priori can be observed that the refined transmission process such as Soft-matting or Guided Image Filtering consumes most of the computation time, i.e., 70% of the execution time[59]. In this paper, we use the following method to estimate transmission.

By 4.1,

$$\mathbf{d}^{\mathbf{I}}(\mathbf{x}) \geq \mathbf{A}_0(1 - \mathbf{t}(\mathbf{x})) \quad (5.1)$$

then

$$\mathbf{t}(\mathbf{x}) \geq 1 - \frac{\mathbf{d}^{\mathbf{I}}(\mathbf{x})}{\mathbf{A}_0} \quad (5.2)$$

when $\mathbf{d}^{\mathbf{J}}(\mathbf{x})\mathbf{t}(\mathbf{x}) \rightarrow 0$, i.e., at the pixels where $\mathbf{d}^{\mathbf{J}}(\mathbf{x}) \rightarrow 0$ (By [3],it often happens) or quite far pixels (out-door images) $\mathbf{t}(\mathbf{x}) \rightarrow 0$,

$$\mathbf{t}(\mathbf{x}) \rightarrow 1 - \frac{\mathbf{d}^{\mathbf{I}}(\mathbf{x})}{\mathbf{A}_0} \quad (5.3)$$

For $S_a \times S_a$ neighborhood $\Omega(\mathbf{x})$ near pixel \mathbf{x} , using Mean filter on both sides of Eq.(5.2)

$$\mathbf{Mean}_{\mathbf{x} \in \Omega(\mathbf{x})}(\mathbf{t}(\mathbf{x})) \geq 1 - \frac{\mathbf{Mean}_{\mathbf{x} \in \Omega(\mathbf{x})}(\mathbf{d}^{\mathbf{I}}(\mathbf{x}))}{\mathbf{A}_0} \quad (5.4)$$

let $\tilde{\mathbf{t}}(\mathbf{x}) = \mathbf{Mean}_{\mathbf{x} \in \Omega(\mathbf{x})}(\mathbf{t}(\mathbf{x}))$ then we get

$$\tilde{\mathbf{t}}(\mathbf{x}) \geq 1 - \frac{\mathbf{Mean}_{\mathbf{x} \in \Omega(\mathbf{x})}(\mathbf{d}^{\mathbf{I}}(\mathbf{x}))}{\mathbf{A}_0} \quad (5.5)$$

we use global hazy degree to estimate the value of $\tilde{\mathbf{t}}(\mathbf{x})$

$$\tilde{\mathbf{t}}(\mathbf{x}) = 1 - \omega \frac{\mathbf{Mean}_{\mathbf{x} \in \Omega(\mathbf{x})}(\mathbf{d}^{\mathbf{I}}(\mathbf{x}))}{\mathbf{A}_0} \quad (5.6)$$

Here, ω is from Eq.(4.12), when ω is large,that is the image is very hazy, in Eq.(5.6), $\tilde{\mathbf{t}}(\mathbf{x})$ become small, then haze will be strongly removed in dehazed image, and vice versa.

By Eq.(5.1) and Eq.(5.6), we set

$$\mathbf{t}(\mathbf{x}) = \max\left(\tilde{\mathbf{t}}(\mathbf{x}), 1 - \frac{\mathbf{d}^{\mathbf{I}}(\mathbf{x})}{\mathbf{A}_0}\right) \quad (5.7)$$

After the transmission map is estimated, the scene radiance can be recovered according to Eq.(4.1), The final scene radiance $\mathbf{J}(\mathbf{x})$ is recovered by

$$\mathbf{J}(\mathbf{x}) = \frac{\mathbf{I}(\mathbf{x}) - \mathbf{A}}{\max(\mathbf{t}(\mathbf{x}), \mathbf{t}_0)} + \mathbf{A} \quad (5.8)$$

The term $\mathbf{J}(\mathbf{x})\mathbf{t}(\mathbf{x})$ can be very close to zero. When the transmission $\mathbf{t}(\mathbf{x})$ is close to zero, which make the recovered scene radiance $\mathbf{J}(\mathbf{x})$ is prone to noise. Therefore, the transmission $\mathbf{t}(\mathbf{x})$ is restricted by a low bound \mathbf{t}_0 , a typical value of \mathbf{t}_0 is 0.1.

5.2 Algorithms and Complexity

The main process of this algorithm is as follows:

1. Input Haze image $\mathbf{I}(\mathbf{x})$;
2. Calculate $\mathbf{d}^{\mathbf{I}}(\mathbf{x})$, d , b , and $\max(\mathbf{b}^{\mathbf{I}}(\mathbf{x}))$;
3. Estimate the dehaze factor ω and \mathbf{A}_0
4. Flitering $\mathbf{d}^{\mathbf{I}}(\mathbf{x})$ using mean filter and calculate $\tilde{\mathbf{t}}(\mathbf{x})$
5. Calculate the transmission $\mathbf{t}(\mathbf{x})$
6. Output the recovered image $\mathbf{J}(\mathbf{x})$

Fig.5.2 gives the flow chart of this method. It can be seen that the time-consuming parts of the whole algorithm is the mean filter in step 4, for an image with $S_x \times S_y$ pixels, other steps can be completed in $O(S_x \times S_y)$. In [60][61], a fast implementation of the mean filter in $O(S_x \times S_y)$ is proposed. Thanks to this fast mean filter, the complexity of the proposed algorithm is also $O(S_x \times S_y)$, i.e, it is a linear function of the number of input image pixels whatever the window size $S_a \times S_a$ of mean filter.

5.3 Experimental Results and Analysis

The proposed method is implemented by using Visual Studio 2010 and OpenCV vision library, and a personal computer DELL Precision M4600 with a 2.80GHz Intel Core

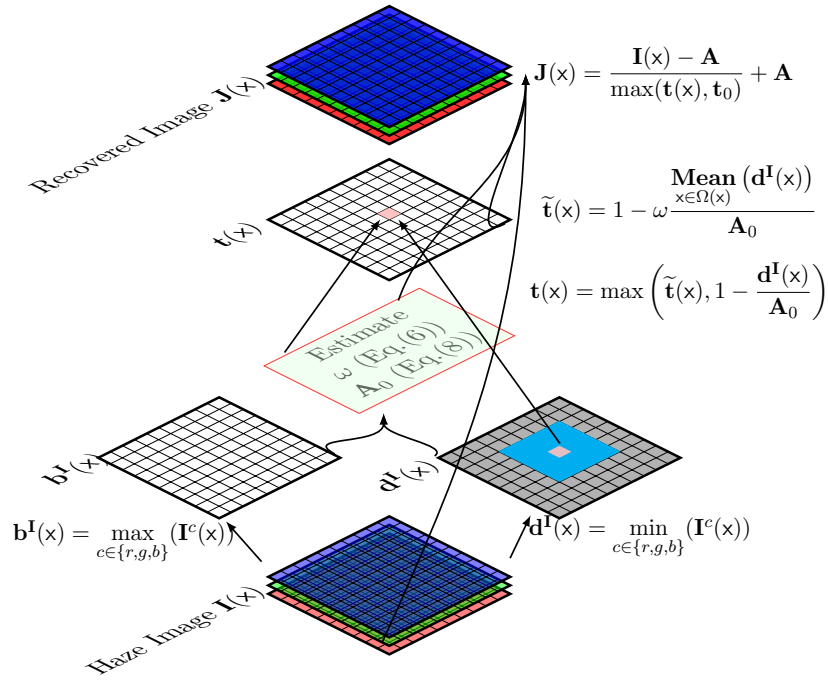


FIGURE 5.1: Algorithm flow of our dehazing method

i7-2640M processor is employed in the test. In this section, to show the effectiveness of our method, we compare it with He's work [3] on both image restoration quality and the time complexity, and examples are given as following.

5.3.1 Image restoration quality

There is no generally accepted method to evaluate the effect of dehazing, a simple evaluating method is proposed by this research. Suppose $\|\mathbf{I}\| = \sqrt{\sum_{x \in \mathbf{x}} \mathbf{I}^2(x)}$, Suppose \mathbf{I} denotes original hazed image, and \mathbf{I}' denotes dehazed-output image, then dehazing factor ρ is defined as:

$$\rho = \frac{\|\mathbf{I} - \mathbf{I}'\|}{\|\mathbf{I}\|}$$

This ρ may represent the differences between dehazed result and original image, however, in some case, for instance color bias happened and over-hazed, the dehazing factor can get higher value. Referring Tab.5.1, Tab.5.2 and Tab.5.3, ρ is not always higher is better, the dehazing factor of Tan's method get extraordinary highest value almost, but the results of his show abnormal high contrast. For the sake of the result of Kopf et al.'08 is believed getting better results of dehazing, the dehazing factor of his is selected as a standard in this thesis.

TABLE 5.1: Our method's image restoration quality compare to others'













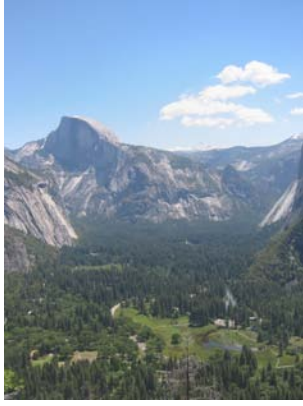

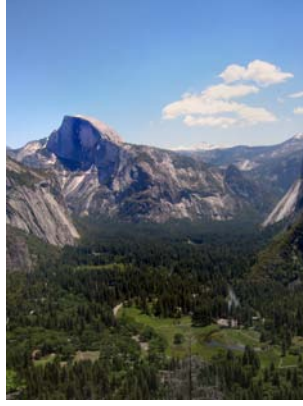
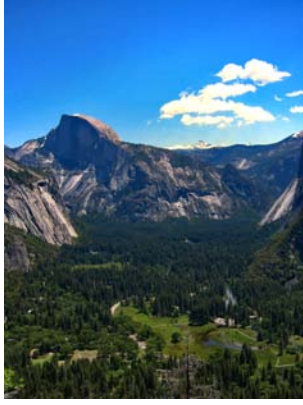

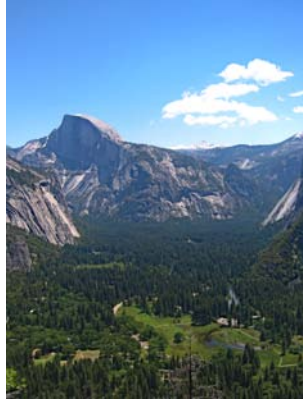
Original	Kopf et al.'08
	
	$\rho = 0.212936$
Fattal'08	He et al.'09
	
$\rho = 0.146794$	$\rho = 0.235055$
Tan'08	ours
	
$\rho = 0.394571$	$\rho = 0.264699$

TABLE 5.2: Our method's image restoration quality compare to others'

Original	Kopf et al.'08	Fattal'08
		
	$\rho = 0.188409$	$\rho = 0.256156$
He et al.'09	Tan'08	ours
		
$\rho = 0.303624$	$\rho = 0.427152$	$\rho = 0.23090$

























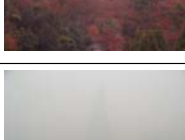


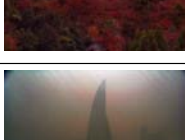
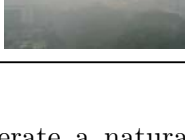
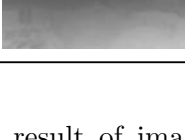


Tab.5.1, Tab.5.2 and Tab.5.3 illustrates the comparisons and dehazing factors of our method with Kopf et al.'08 [30], Fattal'08[5], He et al.'09[3], Tan'08[4]. Kopf's method get the best effect to dehaze, depended a data-driven dehazing procedure, by employing a registration process to align the photograph within an existing 3D model. This way the method does not need to estimate the distances in the scene, assuming that such kind of georeferenced digital terrain and urban models are available. Because of the need of alignment, the method is time-consuming, and does not have the versatility. Tans method can augment the image details and greatly enhance the image visually. However, the colors in the recovered images are often over saturated, since the method is not a physically based approach and the transmission may thus be underestimated. Moreover, some significant halo artifacts usually appear around the recovered sharp

TABLE 5.3: Our method's image restoration quality compare to others'

Original	Kopf et al.'08	Fattal'08
		
	$\rho = 0.20509$	$\rho = 0.232987$
He et al.'09	Tan'08	ours
		
$\rho = 0.36681$	$\rho = 0.412999$	$\rho = 0.185656$

edges (e.g., Buildings far away). In comparison, our method can improve the visibility of image structures in very dense haze regions while restoring the faithful colors. The halo artifacts in our results are also quite small. Fattals method relies on sufficient color information to estimate the transmission. If the haze is very dense, the color information will be very faint and the transmission may thus be wrongly estimated, leading to erroneous enhancement on the image. For example, the bridge enhanced by Fattals method is too dark and some hazes still remain among the Horizon. As can be seen from the results, He's method produce satisfactory results in regions with heavy hazes. In regions far, our method performs better, He's method presence color bias especially the color of the buildings near the bridge looks dim and unnatural. Though hazes remain in our dehazing results, halo artifacts are smaller. Moreover, our method

TABLE 5.4: Our method’s image restoration quality compare to He’s

Image No.	Original image	ω	$[255t(x)]$	Our’s	He’s($\omega = 0.95$)
1		0.5120			
2		0.4682			
3		0.6315			
4		0.4560			
5		0.5171			
6		0.8290			
7		0.3161			
8		0.7613			

tends to generate a natural-looking result of image details. This benefits from the incorporation of a median filter into image dehazing. These filters can help to exploit and augment the interesting image structures, e.g., jump edges and corners. In comparison, our results are much visually pleasing.

He’s method achieve good performance performance in quality and processing speed have good performance. In Tab.5.4, eight images’ restoration quality of our’s method and He’s are shown. Clearly, our treatment effect substantially close to He’s in the area of non-sky. Please note, in the area of sky of Image No.2, 4 , 6 , 8, Dark Channel Prior method result overdehazed and color distortion. Despite the fog remains in distant of our result, but very natural transition exists from near to far.

5.3.2 Enhanced edge detection

Enhanced edge detection affection test is also carried out to evaluate detail-recovering capability. Using Canny detector ($minVal = 50, maxVal = 120, kernelSize = 5$) correspond on iamges in Tab.5.1, Tab.5.2 and Tab.5.3. Tab.5.5, Tab.5.6 and Tab.5.7 illustrates the comparisons of enhanced edge detection affection and ρ of our method with Kopf et al.'08 [30], Fattal'08[5], He et al.'09[3], Tan'08[4]. Similarly to the above conclusions, the dehazed image processed by proposed method can extracte more edges, with the comparable ability with Kopf et al.'08 [30], Fattal'08[5], He et al.'09[3]. Similarly, Tan'08[4] gets the highest ρ in the test, yet might contain a lot of noise.

5.3.3 Processing time cost

Tab.5.8 shows our method has an advantage in terms of processing speed even to improved Dark Channel Prior methods, and we believe there is room for improvement by optimizing algorithm.

5.3.4 Effects of Different scenarios

To test the robustness of our algorithm, we pick up FRIDA images to handle individually. FRIDA is comprised of 90 synthetic images of 18 urban road scenes. Each image is 640×480 pixels. (Mean execution time is 230 ms on an Intel Core I7 CPU.) See Fig.5.2, which shows sample images, Each image without fog (Lima set) is associated four foggy images. Different types of fog are added to each of the four associated images: uniform fog(U080), heterogeneous fog(K080), cloudy fog(L080), and cloudy heterogeneous fog(M080). Tab.5.9 shows the 7th photo's dehaze effect of 5 sets (Lima-000007 is unprocessed), we can see the dehazed images of 4 kinds of haze have natural defogging effect, consistent with the results, no issues to be overdehazed.

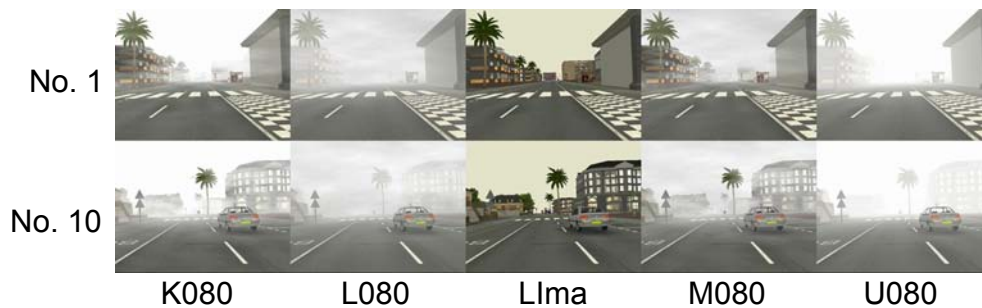


FIGURE 5.2: Sample images from the FRIDA Database

TABLE 5.5: Our method's image enhanced edge detection affection compare to others'


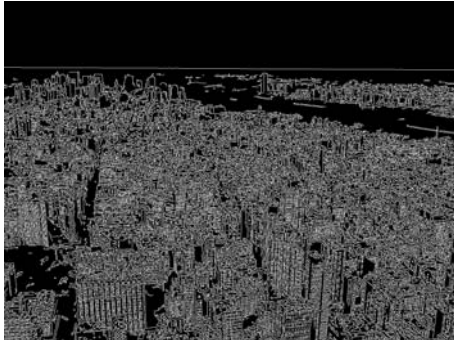
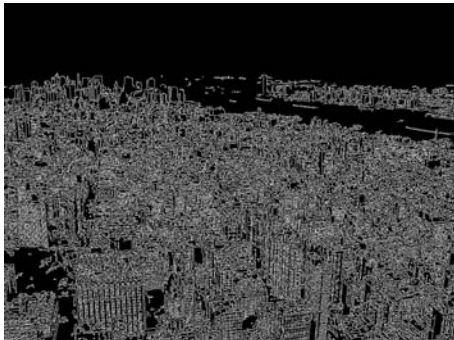
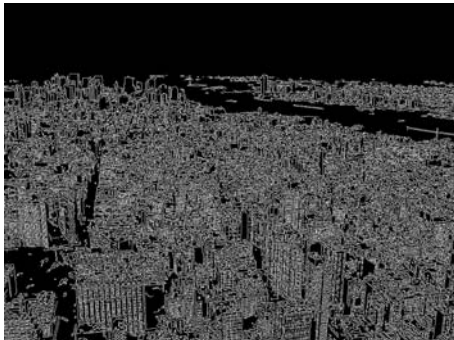
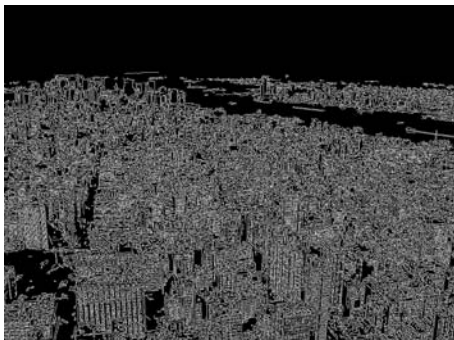
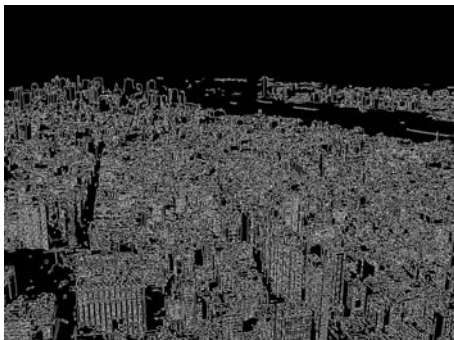
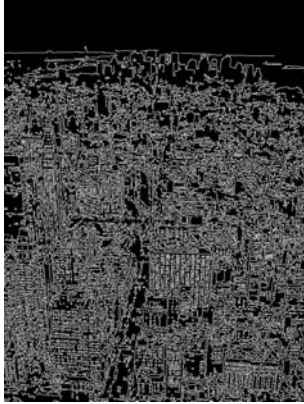
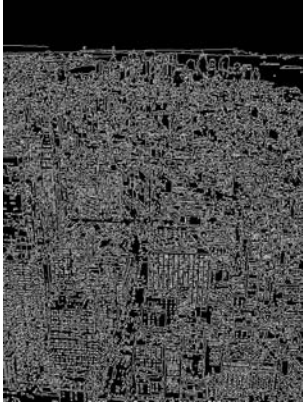
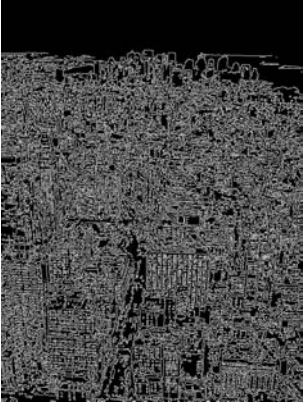
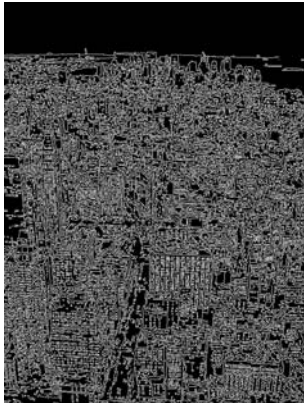
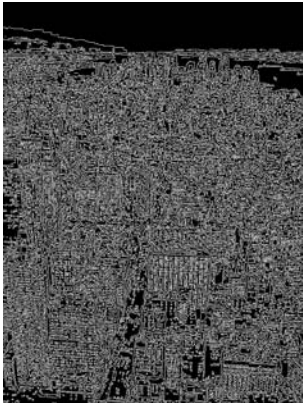
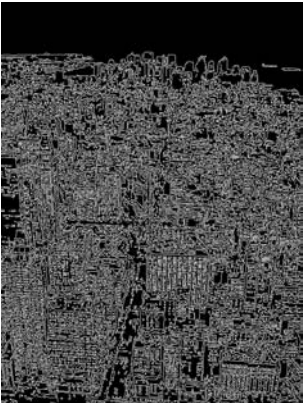
Original	Kopf et al.'08
	
	$\rho = 0.425162$
Fattal'08	He et al.'09
	
$\rho = 0.482821$	$\rho = 0.407717$
Tan'08	ours
	
$\rho = 0.601032$	$\rho = 0.442046$

TABLE 5.6: Our method's image enhanced edge detection affection compare to others'

Original	Kopf et al.'08	Fattal'08
		
	$\rho = 0.487553$	$\rho = 0.502986$
He et al.'09	Tan'08	ours
		
$\rho = 0.422012$	$\rho = 0.661718$	$\rho = 0.503297$

5.4 Application of dehazing and symmetry detection

I propose to use the dehazing method on symmetry detecting[62]. Suppose that the following n points in R^3 (or R^2) are given,

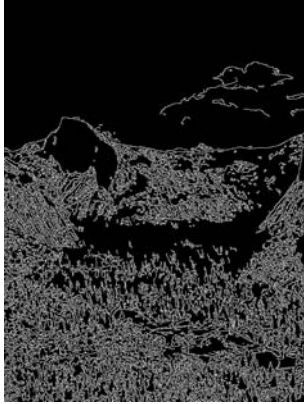
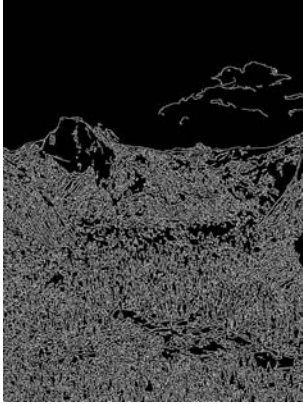
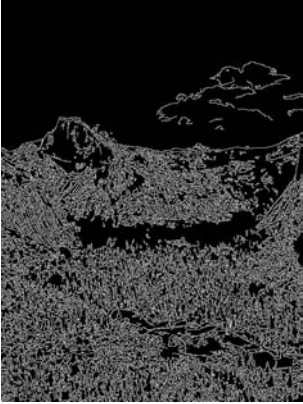
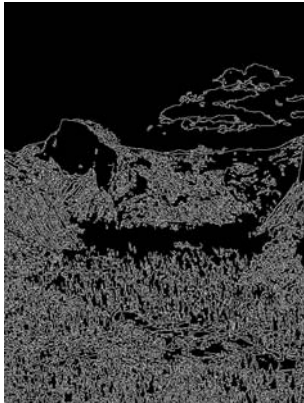
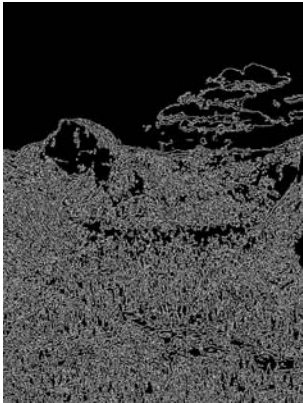
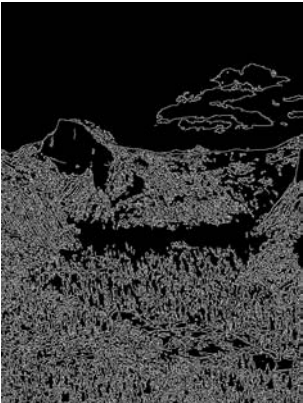
$$\mathbf{p}_1 = (p_{11}, p_{12}, p_{13})^t, \dots, \mathbf{p}_n = (p_{n1}, p_{n2}, p_{n3})^t$$

and

$$\mathbf{p}'_1 = (p'_{11}, p'_{12}, p'_{13})^t, \dots, \mathbf{p}'_n = (p'_{n1}, p'_{n2}, p'_{n3})^t$$

Let $A = (\mathbf{p}_1, \dots, \mathbf{p}_n)$ and $A' = (\mathbf{p}'_1, \dots, \mathbf{p}'_n)$.

TABLE 5.7: Our method's image enhanced edge detection affection compare to others'

Original	Kopf et al.'08	Fattal'08
		
	$\rho = 0.626931$	$\rho = 0.488037$
He et al.'09	Tan'08	ours
		
$\rho = 0.468885$	$\rho = 0.78695$	$\rho = 0.492789$

5.4.1 Definition of $D(AA')$

$$D(AA') = \min \sum_{i=1}^n \sum_{j=1}^n \|\mathbf{p}_i - \mathbf{p}'_j\| x_{ij}$$

$$\text{s.t.} \begin{cases} \sum_{i=1}^n x_{ij} = 1, j = 1, 2, \dots, n \\ \sum_{j=1}^n x_{ij} = 1, i = 1, 2, \dots, n \\ x_{ij} = 0 \text{ or } 1, i, j = 1, 2, \dots, n \end{cases}$$

And suppose that the matrix $\mathbf{X} = [\mathbf{x}_{ij}]$.

5.4.2 Details of A and A'

Suppose that there exists a plane $\pi : \mathbf{w}^t \mathbf{x} = w_0$ in R^3 ,

where $\mathbf{w} = (w_1, w_2, w_3)^t$, $\mathbf{x} = (x_1, x_2, x_3)^t$, $\|\mathbf{w}\| \neq 0$, $w_0 \in R$,

For each point $\mathbf{p}_i \in A$, we can get other point \mathbf{p}'_i where plane π as the Plane of Symmetry. Let $\mathbf{p}'_i \in A'$.

then we can find A' from A and plane $\pi : \mathbf{w}^t \mathbf{x} = w_0$ as follows:

$$\mathbf{u} = \frac{\mathbf{w}}{\|\mathbf{w}\|} \quad (5.9)$$

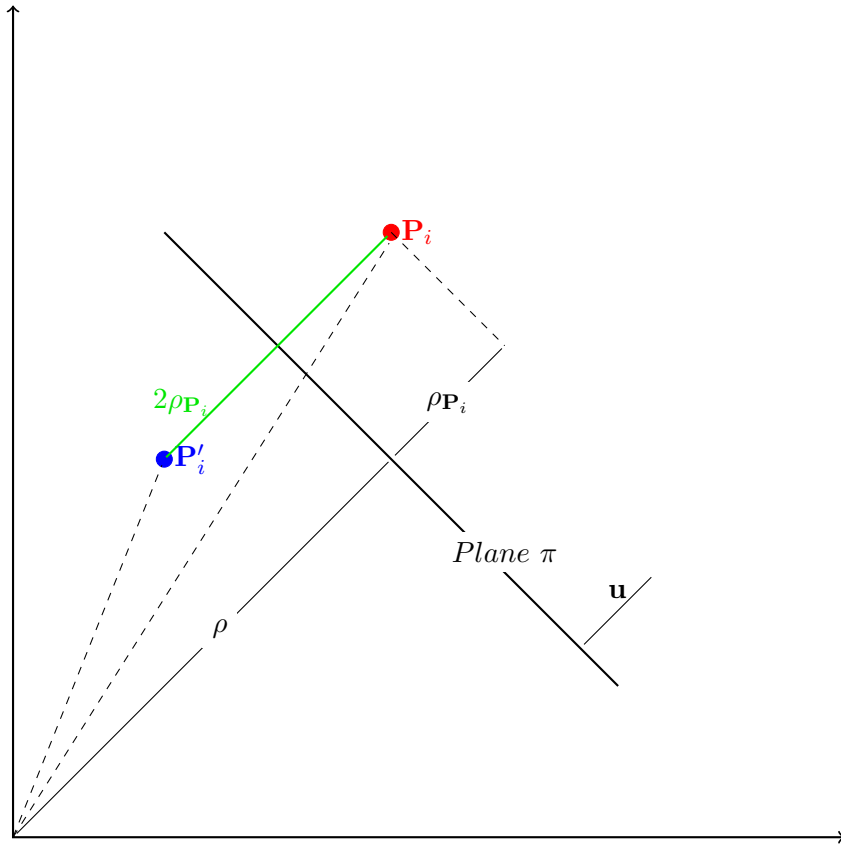
$$\rho = \frac{-w_0}{\|\mathbf{w}\|} \quad (5.10)$$

$$\rho_{\mathbf{p}} = A^t * \mathbf{u} - \rho * \mathbf{e} \quad (5.11)$$

$$A' = A - 2\mathbf{u} * (\rho_{\mathbf{p}})^t \quad (5.12)$$

$$\mathbf{e} = \underbrace{(1, 1, \dots, 1, 1)^t}_n \quad (5.13)$$

- (1) \mathbf{u} is the normal vector of plane π
- (2) ρ is distance from original point to plane π
- (3) $\rho_{\mathbf{p}}$ is a vector, the i th element is distance from the point \mathbf{p}_i to the plane π



Suppose $D(AA') = \varepsilon \geq 0$

if $\varepsilon = 0$,

then the plane π is one of the plane of exactly symmetry

and for some $\varepsilon \geq 0$ sufficiently small, the plane π is the *Plane of ε -approximate Symmetry* of A . I did some comparison test of symmetry detection in original and dehazed images, see Fig.5.3, both images are edge extracted using Canny Edge Detector with $\text{minVal}=50$, $\text{maxVal}=150$, $\text{kernsize}=3$. From original image there is only one target is observed, after dehazing, 4 targets are detected, which shows our dehazing method can be used to reduce noise and increase the visual range.

5.5 Conclusion

In this chapter, a simple but efficient method to improve single image dehazing algorithm based on statistical methods is proposed, which can work well for the various conditions. In the improved method, haze degree can be calculated in advance, and transmission can be refined by mean filter once. Therefore, color distortion and halos in invalid regions can be avoided. Finally, the restored images are obviously more natural, softer and clearer. It proved that our method has strong robustness and high availability, and can be widely applied to the real-time dehazing for videos and actual projects.

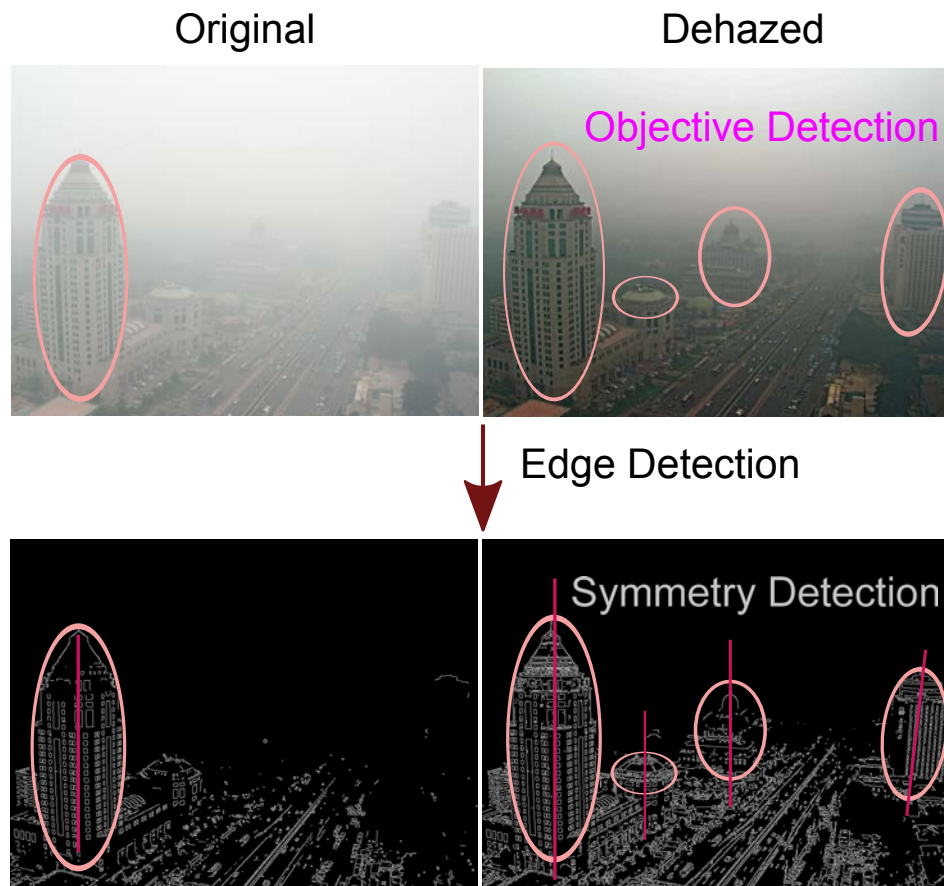












FIGURE 5.3: Sample application of Dehazing and Symmetry detection

TABLE 5.8: Processing time cost compare to He's

Image No.	Image Size	Time cost(ms)	
		Our's	He's
1	800 × 600	1933.79	3746.68
2	800 × 600	1920.82	3997.35
3	800 × 600	1930.76	3595.26
4	1024 × 768	2666.08	4270.92
5	800 × 600	1980.94	3654.60
6	1024 × 768	3615.62	5777.25
7	1024 × 768	3561.33	5072.52
8	1024 × 768	3546.14	5235.01

TABLE 5.9: Effects of Different scenarios

Image No.	Original	processed
K080-000007		
L080-000007		
Lima-000007		
M080-000007		
U080-000007		

Chapter 6

Conclusions and future work

6.1 conclusions

In my work, I described the physical basis for dehazing algorithms and exhibited existing methods. Today's methods are physically sound and produce qualitatively good results, however more attention to dehazing quality rather than the applicability leads to for real-time applications they may not always be fast enough. In this thesis, we present a novel method to detect haze images and label them haze factor with a high identification. This method can be independently used for weather conditions automatic identifying as well as batch images and video dehazing as a preprocessor and dehazing factor.

Not similar to existing dehazing algorithms try to remove the entire haze which may lead to color bias, overall dim, jagged at the edges, halo in sky area etc. our dehazing method aims to reduce the effect of haze. The complexity could be reduced from $O(n^2)$ to $O(n)$. The recovery of the color, clarify and contrast improves significantly. The dehazed image appear like a clear-day scene instead of unnatural recovered images of the other dehazing algorithms which return unnatural black skies.

With higher robustness, our dehazing method is able to adapt to different situations and needs. It has been shown in the tests here that although the method was built with just haze in mind, it is possible to even improve foggy, snowy and rainy scenes. Therefore, possible applications are broad, like outdoor surveillance or on board cameras in vehicles[63]. Some researchers even showed that it is possible to improve underwater imaging and aerial photography with similar, if not the same techniques[64].

6.2 future work

Some problems are leaved for further research.

- Our method is based on simplified haze image model, in order to improve the de-hazing results, more sophisticated atmospheric scattering physical model is needed.
- Gathering more images to extract trends and patterns between image pixel values and transmittance in order to improve haze-degree estimating.
- The assumed incident light source is uniform illumination(sunlight), it need to extend to non-uniform illumination.
- achieving higher processing speed by code optimization in order to meet the real-time processing request.
- Propose a reasonable way to judge the effect of dehazing.

Bibliography

- [1] Hulbert E. O. Optics at atmospheric haze. *J. Opt. Soc. Am.*, 31:467–476, 1941.
- [2] J.E. et al. Manson. *The possible role of gas reactions in the formation of the stratospheric aerosol layer*. In *Chemical Reactions in the Lower and Upper Atmosphere*. Interscience, New York., 1959.
- [3] Kaiming He, Jian Sun, and Xiaoou Tang. Single image haze removal using dark channel prior. *Pattern Analysis and Machine Intelligence, IEEE Transactions on*, 33(12):2341–2353, 2011.
- [4] Robby T Tan. Visibility in bad weather from a single image. In *Computer Vision and Pattern Recognition, 2008. CVPR 2008. IEEE Conference on*, pages 1–8. IEEE, 2008.
- [5] Raanan Fattal. Single image dehazing. In *ACM Transactions on Graphics (TOG)*, volume 27, page 72. ACM, 2008.
- [6] Kaiming He, Jian Sun, and Xiaoou Tang. Guided image filtering. In *Computer Vision–ECCV 2010*, pages 1–14. Springer, 2010.
- [7] Bhabatosh Chanda and Dwijesh Dutta Majumder. *Digital image processing and analysis*. PHI Learning Pvt. Ltd., 2004.
- [8] Harry G Barrow and Jay M Tenenbaum. Interpreting line drawings as three-dimensional surfaces. *Artificial intelligence*, 17(1):75–116, 1981.
- [9] Tony Lindeberg. Edge detection and ridge detection with automatic scale selection. *International Journal of Computer Vision*, 30(2):117–156, 1998.
- [10] Wei Zhang and Fredrik Bergholm. Multi-scale blur estimation and edge type classification for scene analysis. *International Journal of Computer Vision*, 24(3):219–250, 1997.
- [11] John Canny. A computational approach to edge detection. *Pattern Analysis and Machine Intelligence, IEEE Transactions on*, (6):679–698, 1986.

-
- [12] Robert M Haralick. Digital step edges from zero crossing of second directional derivatives. *Pattern Analysis and Machine Intelligence, IEEE Transactions on*, (1):58–68, 1984.
- [13] Ron Kimmel and Alfred M Bruckstein. Regularized laplacian zero crossings as optimal edge integrators. *International Journal of Computer Vision*, 53(3):225–243, 2003.
- [14] Rachid Deriche. Using canny’s criteria to derive a recursively implemented optimal edge detector. *International journal of computer vision*, 1(2):167–187, 1987.
- [15] Lord Rayleigh. Xxxiv. on the transmission of light through an atmosphere containing small particles in suspension, and on the origin of the blue of the sky. *The London, Edinburgh, and Dublin Philosophical Magazine and Journal of Science*, 47(287):375–384, 1899.
- [16] Mark Z Jacobson. *Fundamentals of atmospheric modeling*. Cambridge University Press, 2005.
- [17] AJ Cox, Alan J DeWeerd, and Jennifer Linden. An experiment to measure mie and rayleigh total scattering cross sections. *American Journal of Physics*, 70(6):620–625, 2002.
- [18] G. Mie. Beiträge zur Optik trüber Medien, speziell kolloidaler Metallösungen. *Annalen der Physik*, 330:377–445, 1908. doi: 10.1002/andp.19083300302.
- [19] Hendrik Christoffel Hulst and HC Van De Hulst. *Light scattering by small particles*. Courier Dover Publications, 1957.
- [20] Fabio Cozman and Eric Krotkov. *Depth from scattering*. 1997.
- [21] Earl J McCartney. Optics of the atmosphere: scattering by molecules and particles. *New York, John Wiley and Sons, Inc., 1976. 421 p., 1*, 1976.
- [22] MCW van van Rossum and Th M Nieuwenhuizen. Multiple scattering of classical waves: microscopy, mesoscopy, and diffusion. *Reviews of Modern Physics*, 71(1):313, 1999.
- [23] Harald Koschmieder. *Theorie der horizontalen Sichtweite: Kontrast und Sichtweite*. Keim & Nemnich, 1925.
- [24] WK Middleton. Vision through the atmosphere. 1952.
- [25] Pat S Chavez Jr. An improved dark-object subtraction technique for atmospheric scattering correction of multispectral data. *Remote sensing of environment*, 24(3):459–479, 1988.

- [26] Srinivasa G Narasimhan and Shree K Nayar. Interactive (de) weathering of an image using physical models. In *IEEE Workshop on Color and Photometric Methods in Computer Vision*, volume 6, page 1. France, 2003.
- [27] Yoav Y Schechner, Srinivasa G Narasimhan, and Shree K Nayar. Polarization-based vision through haze. *Applied Optics*, 42(3):511–525, 2003.
- [28] Sarit Shwartz, Einav Namer, and Yoav Y Schechner. Blind haze separation. In *Computer Vision and Pattern Recognition, 2006 IEEE Computer Society Conference on*, volume 2, pages 1984–1991. IEEE, 2006.
- [29] Ran Kaftory, Yoav Y Schechner, and Yehoshua Y Zeevi. Variational distance-dependent image restoration. In *Computer Vision and Pattern Recognition, 2007. CVPR'07. IEEE Conference on*, pages 1–8. IEEE, 2007.
- [30] Johannes Kopf, Boris Neubert, Billy Chen, Michael Cohen, Daniel Cohen-Or, Oliver Deussen, Matt Uyttendaele, and Dani Lischinski. Deep photo: Model-based photograph enhancement and viewing. In *ACM Transactions on Graphics (TOG)*, volume 27, page 116. ACM, 2008.
- [31] J-P Tarel, Nicolas Hautière, Laurent Caraffa, Aurélien Cord, Houssam Halmaoui, and Dominique Gruyer. Vision enhancement in homogeneous and heterogeneous fog. *Intelligent Transportation Systems Magazine, IEEE*, 4(2):6–20, 2012.
- [32] Yoav Y Schechner and Nir Karpel. Recovering scenes by polarization analysis. In *OCEANS'04. MTTs/IEEE TECHNO-OCEAN'04*, volume 3, pages 1255–1261. IEEE, 2004.
- [33] Jiafeng Li, Hong Zhang, Ding Yuan, and Helong Wang. Haze removal from single images based on a luminance reference model. In *Pattern Recognition (ACPR), 2013 2nd IAPR Asian Conference on*, pages 446–450. IEEE, 2013.
- [34] Deepak Kumar Naik and Deepak Kumar Rout. Outdoor image enhancement: Increasing visibility under extreme haze and lighting condition. In *Advance Computing Conference (IACC), 2014 IEEE International*, pages 1081–1086. IEEE, 2014.
- [35] Srinivasa G Narasimhan and Shree K Nayar. Vision and the atmosphere. *International Journal of Computer Vision*, 48(3):233–254, 2002.
- [36] Srinivasa G. Narasimhan and Shree K. Nayar. Contrast restoration of weather degraded images. *Pattern Analysis and Machine Intelligence, IEEE Transactions on*, 25(6):713–724, 2003.

- [37] Louis Kratz and Ko Nishino. Factorizing scene albedo and depth from a single foggy image. In *Computer Vision, 2009 IEEE 12th International Conference on*, pages 1701–1708. IEEE, 2009.
- [38] J-P Tarel and Nicolas Hautiere. Fast visibility restoration from a single color or gray level image. In *Computer Vision, 2009 IEEE 12th International Conference on*, pages 2201–2208. IEEE, 2009.
- [39] Jing Yu, Chuangbai Xiao, and Dapeng Li. Physics-based fast single image fog removal. In *Signal Processing (ICSP), 2010 IEEE 10th International Conference on*, pages 1048–1052. IEEE, 2010.
- [40] Ko Nishino, Louis Kratz, and Stephen Lombardi. Bayesian defogging. *International journal of computer vision*, 98(3):263–278, 2012.
- [41] Jing Yu and Qingmin Liao. Fast single image fog removal using edge-preserving smoothing. In *Acoustics, Speech and Signal Processing (ICASSP), 2011 IEEE International Conference on*, pages 1245–1248. IEEE, 2011.
- [42] Cosmin Ancuti, Codruta Ormiana Ancuti, Tom Haber, and Philippe Bekaert. Enhancing underwater images and videos by fusion. In *Computer Vision and Pattern Recognition (CVPR), 2012 IEEE Conference on*, pages 81–88. IEEE, 2012.
- [43] Bin Xie, Fan Guo, and Zixing Cai. Improved single image dehazing using dark channel prior and multi-scale retinex. In *Intelligent System Design and Engineering Application (ISDEA), 2010 International Conference on*, volume 1, pages 848–851. IEEE, 2010.
- [44] Inhye Yoon, Seonyung Kim, Donggyun Kim, Monson H Hayes, and Joonki Paik. Adaptive defogging with color correction in the hsv color space for consumer surveillance system. *Consumer Electronics, IEEE Transactions on*, 58(1):111–116, 2012.
- [45] Chao-Tsung Chu and Ming-Sui Lee. A content-adaptive method for single image dehazing. In *Advances in Multimedia Information Processing-PCM 2010*, pages 350–361. Springer, 2011.
- [46] Mengyang Chen, Aidong Men, Peng Fan, and Bo Yang. Single image defogging. In *Network Infrastructure and Digital Content, 2009. IC-NIDC 2009. IEEE International Conference on*, pages 675–679. IEEE, 2009.
- [47] Nachiket Desai, Aritra Chatterjee, Shaunak Mishra, Dhaval Chudasama, Sunav Choudhary, and Sudhir Kumar Barai. A fuzzy logic based approach to de-weather fog-degraded images. In *Computer Graphics, Imaging and Visualization, 2009. CGIV'09. Sixth International Conference on*, pages 383–387. IEEE, 2009.

- [48] Erik Matlin and Peyman Milanfar. Removal of haze and noise from a single image. In *IS&T/SPIE Electronic Imaging*, pages 82960T–82960T. International Society for Optics and Photonics, 2012.
- [49] Haoran Xu, Jianming Guo, Qing Liu, and Lingli Ye. Fast image dehazing using improved dark channel prior. In *Information Science and Technology (ICIST), 2012 International Conference on*, pages 663–667. IEEE, 2012.
- [50] Charles Poynton. *Digital video and HD: Algorithms and Interfaces*. Elsevier, 2012.
- [51] Einav Namer and Yoav Y Schechner. Advanced visibility improvement based on polarization filtered images. In *Optics & Photonics 2005*, pages 588805–588805. International Society for Optics and Photonics, 2005.
- [52] Shree K Nayar and Srinivasa G Narasimhan. Vision in bad weather. In *Computer Vision, 1999. The Proceedings of the Seventh IEEE International Conference on*, volume 2, pages 820–827. IEEE, 1999.
- [53] Peter Carr and Richard Hartley. Improved single image dehazing using geometry. In *Digital Image Computing: Techniques and Applications, 2009. DICTA '09.*, pages 103–110. IEEE, 2009.
- [54] Martin Roser and Frank Moosmann. Classification of weather situations on single color images. In *Intelligent Vehicles Symposium, 2008 IEEE*, pages 798–803. IEEE, 2008.
- [55] Mario Pavlic, Heidrun Belzner, Gerhard Rigoll, and Slobodan Ilic. Image based fog detection in vehicles. In *Intelligent Vehicles Symposium (IV), 2012 IEEE*, pages 1132–1137. IEEE, 2012.
- [56] Sebastián Bronte, Luis M Bergasa, and Pablo F Alcantarilla. Fog detection system based on computer vision techniques. In *Intelligent Transportation Systems, 2009. ITSC'09. 12th International IEEE Conference on*, pages 1–6. IEEE, 2009.
- [57] Zichong Chen, Feng Yang, Albrecht Lindner, Guillermo Barrenetxea, and Martin Vetterli. How is the weather: Automatic inference from images. In *Image Processing (ICIP), 2012 19th IEEE International Conference on*, pages 1853–1856. IEEE, 2012.
- [58] J-P Tarel, Nicolas Hautiere, Aurélien Cord, Dominique Gruyer, and Houssam Halmoui. Improved visibility of road scene images under heterogeneous fog. In *Intelligent Vehicles Symposium (IV), 2010 IEEE*, pages 478–485. IEEE, 2010.
- [59] Nai-Cyun Ke and Ju-Chin Chen. Real-time visibility restoration from a single image.

-
- [60] Ke-jun WANG, Xin-yan XIONG, and Zhen REN. Highly efficient mean filtering algorithm. *Application Research of Computers*, 2:007, 2010.
- [61] LI Zhang, Zhiqiang Chen, Wenhuan Gao, and KJ Kang. Mean-based fast median filter. *JOURNAL-TSINGHUA UNIVERSITY*, 44(9):1157–1159, 2004.
- [62] Jun Mao and Hiroyuki Shioya. A refinement of extracting approximate symmetry planes based on least square. *Journal of Computer and Communications*, 2(04):188, 2014.
- [63] Nicolas Hautiere and Didier Aubert. Contrast restoration of foggy images through use of an onboard camera. In *Intelligent Transportation Systems, 2005. Proceedings. 2005 IEEE*, pages 601–606. IEEE, 2005.
- [64] Yoav Y Schechner and Nir Karpel. Clear underwater vision. In *Computer Vision and Pattern Recognition, 2004. CVPR 2004. Proceedings of the 2004 IEEE Computer Society Conference on*, volume 1, pages I–536. IEEE, 2004.

Acknowledgements

At this point I would like to thank the people that helped me producing this thesis.

First, I would like to express the deepest gratitude to my advisers, Prof. Kenichi Itakura, Associate Prof. Shinya Watanabe, and Prof. Hiroyuki Shioya , for giving me the opportunity to write this thesis and supporting me along the way, for their excellent guidance, caring, patience, and providing me with an excellent atmosphere for doing research.

I owe a debt of gratitude to Mr. and Mrs. Shiozaki and staffs of the Center of International Relations for their always kind concern and courage.

Many thanks to Ms. Kawada , Mr. Phommasak Uthai, Mr.Izawa tarou, Mr. Phlavanh souphaxay, Mr.Ishihashi katsuya, Ms.sakizawa manami, Mr.morimoto youhei, Mr. Wisan dhammatorn and other members of Shioya Laboratory, for their cooperation and constructive discussion.

I would like to thank Muroran Institute University and Henan Polytechnic University for giving me the opportunity to study.

Everlastingly gratitude to my mife and my son who support and encourage me during my study.

Special thanks go to the members of Tennipon club, and the staffs futsal club of Muroran-IT, playing with you every week refresh myself and dispel my lonely feeling. Your gentle and all out impressed me so much.

Last but not least, I thank people of Muroran, especially Mr. and Mrs. Kiguchi, Mr. and Mrs. Suzuki, Ms. Mari Nakamura, Et al. for providing me enthusiastic help and first-rate study environment.